UNIVERSIDADE FEDERAL DE PERNAMBUCO
CENTRO DE CIÊNCIAS EXATAS E DA NATUREZA
PROGRAMA DE PÓS-GRADUAÇÃO EM FÍSICA

HIGO DE ARAUJO OLIVEIRA

Thermal conductivity calculation in Si membranes:
a Homogeneous Non-Equilibrium Molecular Dynamics approach

Recife

2023

HIGO DE ARAUJO OLIVEIRA

Thermal conductivity calculation in Si membranes:
a Homogeneous Non-Equilibrium Molecular Dynamics approach

Dissertação apresentada ao Programa de Pós-Graduação em Física da Universidade Federal de Pernambuco, como requisito parcial para obtenção do título de mestre em Física. Área de concentração: Física da Matéria condensada e de Materiais.

Orientador (a): Luiz Felipe Cavalcanti Pereira

Recife

2023

Catalogação na fonte
Bibliotecária Nataly Soares Leite Moro, CRB4-1722

O48t Oliveira, Higo de Araujo
Thermal conductivity calculation in Si membranes: a homogeneous non-equilibrium molecular dynamics approach / Higo de Araujo Oliveira. – 2023.
73 f.: il., fig., tab.

Orientador: Luiz Felipe Cavalcanti Pereira.
Dissertação (Mestrado) – Universidade Federal de Pernambuco. CCEN, Física, Recife, 2023.
Inclui referências.

1. Física da matéria condensada e de materiais. 2. Membranas de silício. 3. Condutividade térmica. 4. Fonôns. I. Pereira, Luiz Felipe Cavalcanti (orientador). II. Título.

530.41 CDD (23. ed.) UFPE- CCEN 2023 - 162

HIGO DE ARAUJO OLIVEIRA

THERMAL CONDUCTIVITY CALCULATION IN SI MEMBRANES: A HOMOGENEOUS NON-EQUILIBRIUM MOLECULAR DYNAMICS APPROACH

Dissertação apresentada ao Programa de Pós-Graduação em Física da Universidade Federal de Pernambuco, como requisito parcial para a obtenção do título de Mestre em Física.

Aprovada em: 21/09/2023.

BANCA EXAMINADORA

_____

Prof. Dr. Luiz Felipe Cavalcanti Pereira
Orientador
Universidade Federal de Pernambuco

_____

Prof. Dr. Renê Rodrigues Montenegro Filho
Examinador Interno
Universidade Federal de Pernambuco

_____

Prof. Dr. Davide Donadio
Examinador Externo
University of California, Davis

ACKNOWLEDGEMENTS

First and foremost, I would like to express my gratitude to CNPQ (161927/2021-1) by the fundings, which was essential in sustaining my research journey. Without it, keep pursuing postgraduate studies would have been exceedingly challenging. I would also like to extend my thanks to Professor Luiz Felipe. Despite my background in a different field, chemistry, Luiz welcomed me into the physics department and willingly agreed to be my research advisor. This highlights his understanding of the significance of multidisciplinarity and its role in promoting high-quality scientific development in our country. Also, he always made himself available to listen, clarify doubts, and discuss our research findings.

I would also like to acknowledge Franklin for his companionship. As a fellow chemist and my only other colleague in our still-small group focused on transport in nanostructures within the physics department at UFPE, his partnership was essential. Finally, I want to express my appreciation to my other physicist friends, Alex Ferreira, Allison Rodrigo, and Céfalo Habakuk, individuals I had known since my undergraduate years in chemistry. Both their presence and discussions we had during the Master's courses was essential to my development in physics. Each one of them in some way provided me support in navigating challenges both related and unrelated to science over this entire period.

ABSTRACT

In this work, we calculated the thermal conductivity in the 110 direction of Si membranes with a thickness of a single unit cell (5.431 Angstrom), using the homogeneous non-equilibrium molecular dynamics method. The calculated conductivity using this method for these membranes exhibits a size dependence with respect to to the x, y plane dimensions, but shows convergence for sizes larger than $L \times L$ with $L = 30.72$ nm. The conductivity is found to be 61.73 W/m/K. We also employed the spectral decomposition method of heat flux to separate the average contribution of vibrational modes (phonons) to thermal conductivity. This analysis revealed that the major contribution comes from low-frequency modes ($f \leq 4.5$ THz). Additionally, decomposing the conductivity into in-plane and out-of-plane components allows us to show that the in-plane components (longitudinal and transverse acoustic modes) are the predominant ones. It was observed that the introduction of periodic defects in these membranes reduces the conductivity value by around 90% . This reduction also depends on the defect's geometrical shape. We tested circular, square, and equilateral triangle shapes for the same removed material density (different shapes with same area). The reduction is approximately 90% for squares ($\kappa = 6.037$ W/m/K) and circles ($\kappa = 6.116$ W/m/K), while it is 95% for triangles ($\kappa = 3.290$ W/m/K). This suggests that the phonon scattering at the defect interface depends not only on the removed material density, as already known in literature, but also on the geometric shape of the inserted defects.

Keywords: silicon membranes; thermal conductivity; phonons; defects; molecular dynamics.

RESUMO

Neste trabalho calculamos a condutividade térmica na direção 110 de membranas de Si com espessura de uma única célula unitária (5.431 Angstrom), usando o método de dinâmica molecular homogênea de não-equilíbrio. A condutividade calculada por esse método para essas membranas apresenta dependência com o tamanho no plano x,y, mas mostra convergência para tamanhos maiores do que $L \times L$ com $L = 30.72$ nm, sendo a condutividade dada por 61.73 W/m/K. Também usamos o método de decomposição espectral do fluxo de calor, para separar a contribuição média dos modos vibracionais (fônons) para a condutividade, o que nos mostra que a maior contribuição vem dos modos de baixa frequência ($f \leq 4.5$ THz). Além disso a decomposição da condutividade em componentes dentro e fora do plano, nos permite mostrar que as componentes dentro do plano (modos acústicos longitudinais e transversais) são predominantes. Observamos ainda que a inserção de defeitos periódicos nessas membranas, reduz em cerca 90% o valor da condutividade. Essa redução depende também do formato do defeito. Testamos formatos circulares, quadrados e triangulos equiláteros, para uma mesma densidade de material removido (formas com a mesma área). A redução é cerca de 90% para quadrados ($\kappa = 6.037$ W/m/K) e círculos ($\kappa = 6.116$ W/m/K), mas é de 95% para os triângulos ($\kappa = 3.290$ W/m/K). O que indica que o espalhamento dos fônons na interface dos defeitos depende não só da densidade de material removido, como já é conhecido na literatura, mas também da forma geométrica dos defeitos inseridos.

Palavras-chave: membranas de silício; condutividade térmica; fonôns; defeitos; dinâmica molecular.

LIST OF ABBREVIATIONS AND ACRONYMS

BTE	Boltzmann Transport Equation
BZ	Brillouin Zone
EDIP	Enviroment-Dependent Interatomic Potential
EMD	Equilibrium Molecular Dynamics
GPUMD	Graphics Processing Units Molecular Dynamics
HNEMD	Homogeneous Non Equilibrium Molecular Dynamics
LAMMPS	Large-scale Atomic Molecular Massively Parallel Simulator
MD	Molecular Dynamics
MOSFETs	Metal Oxide Field Effect Transistors
NEMD	Non Equilbrium Molecular Dynamics
NIST	National Insitute of Standards and Technology
PNCs	Phononic Crystals
rNEMD	reverse Non Equilibrium Molecular Dynamics

CONTENTS

1 THERMAL PROPERTIES AND APPLICATIONS OF SILICON MATERIALS

Bulk Silicon crystals which crystallize in diamond structure, illustrated in Fig. 1b, are known to be good heat conductors ($\kappa > 100$ $\text{Wm}^{-1}\text{K}^{-1}$) with heat conductivity $\kappa = 148$ $\text{Wm}^{-1}\text{K}^{-1}$ at room temperature (300K) [1]. Bulk silicon has a volume thermal expansion coefficient $\alpha_v = 9 \times 10^{-6}\text{K}^{-1}$, which is considered low. Typically, metallic materials have higher thermal expansion coefficient values with gold being the smallest of them $\alpha_v < 42.6 \times 10^{-6}\text{K}^{-1}$ [2]. This indicates that bulk silicon undergoes minimal expansion or contraction when exposed to temperature changes. This property makes this material an excellent choice for high-temperature applications where dimensional stability is crucial, such as in electronic devices' thermal management systems.

Figure 1 – (a) a-SiO_2 crystal structure and (b) Bulk Silicon diamond structure.

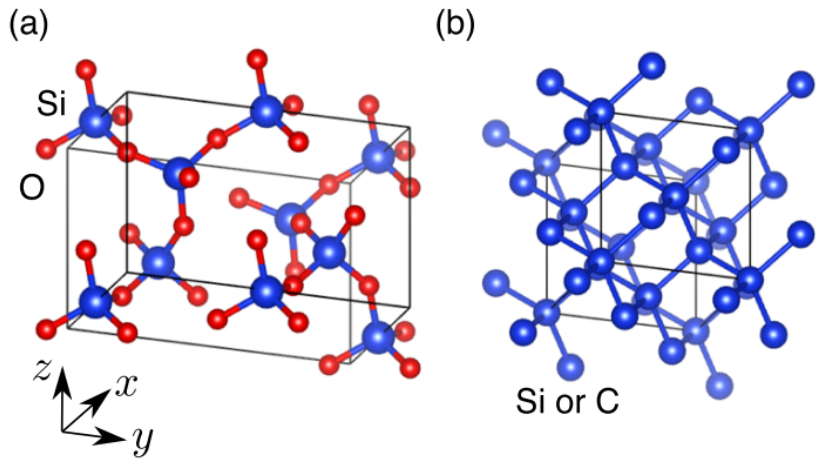

Source: M. Uemoto *et. al* (2019) [3]

Silicon is also commonly used in photovoltaic devices, which convert sunlight into electricity. The first photovoltaic cell made of silicon was created at Bell Labs in 1954 [4]. One of the crucial factors for efficient photovoltaic devices, is heat dissipation. In fact, temperature loss is the dominant factor for decrease in photovoltaic's efficiency [5]. Then, its clear that a material with a high thermal conductivity allows heat to be dissipated more efficiently, which can help prevent overheating and degradation of the device's performance. Therefore, the thermal conductivity of silicon plays a critical role in the efficiency and long-term stability of photovoltaic devices.

In addition to bulk silicon, other forms of silicon such as silicon dioxide (SiO_2) have important electronic applications. Silicon dioxide, presented in Fig. 1a, is an electrical insulator used

in microelectronics as an intermediate layer material between conductive materials. Amorphous films of SiO_2 have a low thermal conductivity ranging from 0.8 to 2.2 $Wm^{-1}K^{-1}$ (depending on the film thickness), which is much lower than that of bulk silicon [6]. This low thermal conductivity makes SiO_2 an excellent insulating material for microelectronics, where it is often used as a dielectric layer between good electrical conductor materials. Its low thermal conductivity allows it to effectively block the transfer of heat between the conductive materials, preventing overheating and damage.

Silicon carbide (SiC) is a highly sought-after silicon-based material in high-temperature applications such as thermal management systems and power electronics. It possesses a significantly higher bandgap of 2.9 eV for 6H-SiC polytype when compared to bulk silicon's 1.1 eV, making it ideal for high-frequency applications [7]. In addition, SiC's larger breakdown voltage of 4 MV/cm, surpasses that of silicon (and 0.3 MV/cm), allowing it to be utilized in microelectronic Metal Oxide Field Effect Transistors (MOSFETs) operating at much higher voltages than pure silicon [7, 8].

Figure 2 – SiC structures (a) 3C and 6H polytypes (blue means carbon and yellow means Si atoms) and (b) 4H polytype, k means quasi-cubic sites and h quasi-hexagonal sites (yellow means Si and black means C atoms).

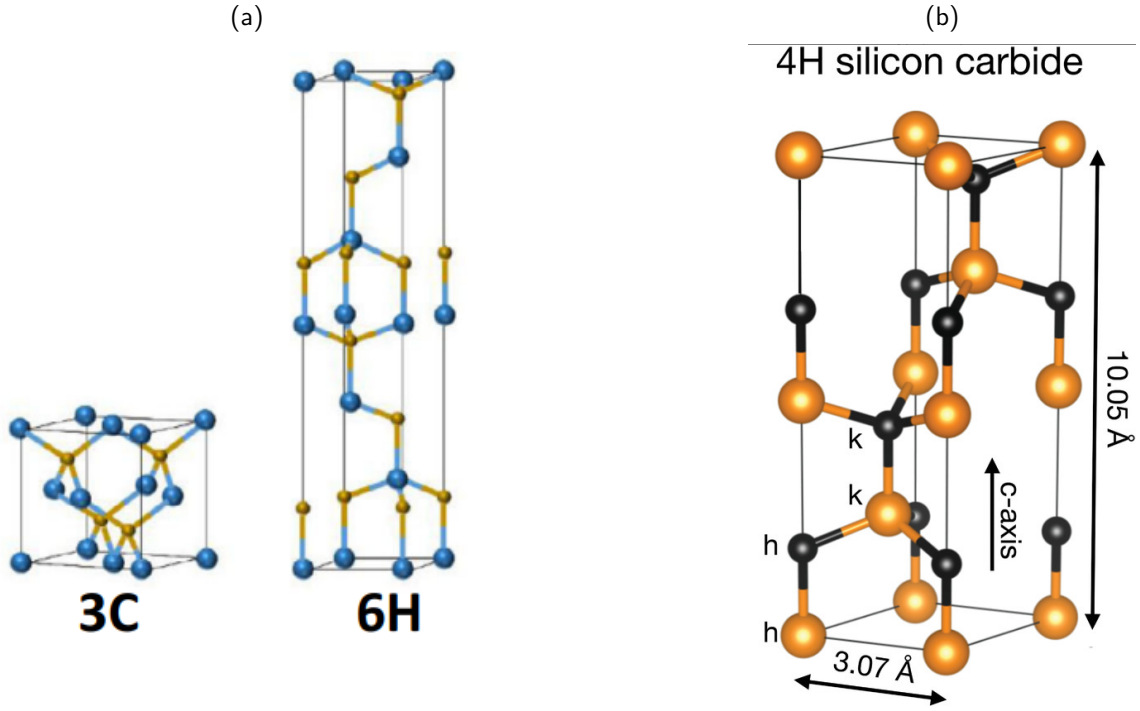

Sources: (a) Zhe Cheng *et. al* (2022) [6] and (b) M. O. de Vries et. al (2021) [9]

What sets SiC apart from other materials is its exceptional thermal conductivity, ranging from 300 to 500 $Wm^{-1}K^{-1}$ at room temperature, depending on the polytype considered [6].

This thermal conductivity is significantly higher than that of SiO_2 and even surpasses that of bulk silicon. Additionally, SiC exhibits excellent mechanical and chemical properties, which make it a highly reliable and versatile material in high-temperature applications.

The thermal conductivity of SiC can vary depending on its crystal structure. SiC has several polytypes, including 3C-SiC and 6H-SiC both showed in Fig. 2a and also 4H-SiC in Fig. 2b, which have different crystal structures and thermal conductivities. The polytypes 4H-SiC and 6H-SiC show anisotropic heat conductivity values and both of them shows hexagonal symmetry. For the direction parallel to the c-axis of symmetry (out of plane) 4H-SiC and 6H-SiC show heat conductivities of 345 and 320 $Wm^{-1}K^{-1}$, respectively. For the direction perpendicular to the c-axis (in plane) direction the values are 415 and 390 $Wm^{-1}K^{-1}$ [10]. The 3C-SiC form shows cubic symmetry and an isotropic heat conductivity value of 500 $Wm^{-1}K^{-1}$, the highest between the three kind of polytypes [6]. These high thermal conductivities make SiC a valuable material for applications where efficient heat dissipation is crucial.

While it has been previously pointed out that the thermal conductivity of silicon (Si) materials can be drastically altered by chemical bonding with other atoms such as oxygen (O) and carbon (C), it is not always necessary to engage in such processes in order to achieve changes in Si's thermal properties. In fact, conductivity reduction can be achieved using pure Si crystals. By utilizing two-dimensional (2D) silicon membranes instead of infinite bulk systems, a drastic reduction of silicon heat conductivity can be obtained, when compared to its bulk value [11].

1.1 TWO DIMENSIONAL MEMBRANES

It is known that phonon scattering is the responsible for heat conductivity reduction in solid materials. In the specific case of 2D membranes, as the thickness dimension it is much smaller than the other two it is expected that boundary scattering in this direction contributes more for heat conductivity reduction. The dimensionality reduction also affects the group velocity of phonons in the smallest direction of these Si membrane, which also contributes to decrease in thermal conductivity. [11, 12] Heat conductivity shows to be a monotonically decreasing function of membrane thickness, as Neogi and Donadio showed on their paper, reprinted in Fig 3. This effect is general and only has to do with the size reduction of the boundaries rather than the material being studied, as Anufriev et. al verified the same functional behavior for membranes made of SiC [12]. Another strategy to further decrease the conductivity of such

Figure 3 – Normalized heat conductivity for Si as a function of membrane thickness. Note that heat conductivity is a monotonically decreasing function of membrane thickness

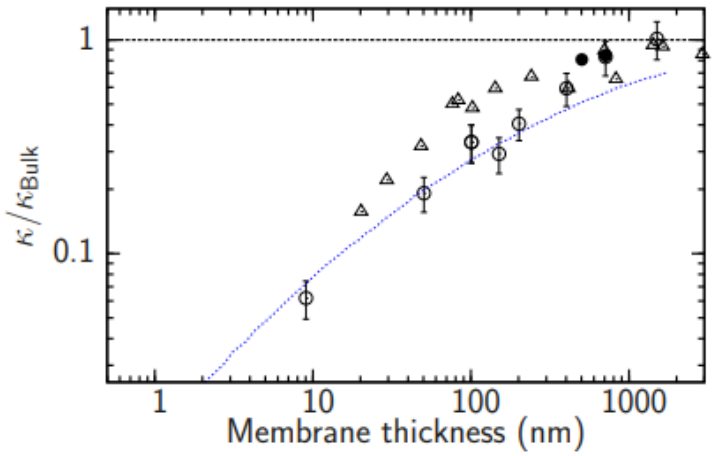

Source: Neogi and Donadio (2015) [11]

membranes is to explore the concept of Phononic Crystals (PNCs).

1.2 PHONONIC CRYSTALS

In recent years PNCs have gained a lot of attention. The idea of PNCs is to modify an existing material considered as the matrix by introducing periodically arranged defects made of another material with different physical properties. On Fig. 4 there is an illustration of a

Figure 4 – Example of a generic phonic crystal membrane with periodicity **a**

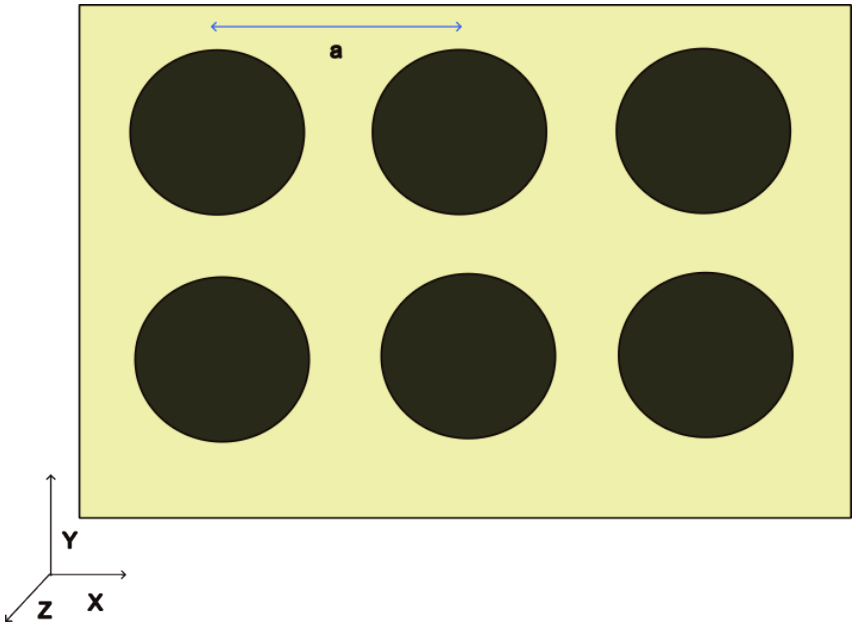

Source: The author (2023)

generic PNC with circular defects. It has been verified that this type of combination creates the possibility of zone folding behavior. That is, the phonon density of states exhibit gaps into some ranges of frequency. Which is equivalent to say that the dispersion relations for the phonons are modified in such a way that some frequencies do not contribute to the density of states inside the first Brillouin Zone (BZ), as showed in Fig. 5 [14, 15]. These band gaps are important because they spam different frequency ranges of the spectrum going from audible sound (20 Hz to 20 KHz [16]), to kHz [17], to MHz [18] and more recently even a few GHz [19] where photonic aplications are also important. The complete absence of mechanical vibration into a given frequency range gives the most obvious application that is to use these PNCs as physical filters of waves, for example. The not so obvious application is related to thermal conductivity reduction. The lower frequency modes of a material (at room temperature) are the ones that contribute the most to the lattice thermal conductivity. If the gap happens to be in some region that affects this low frequency modes, the absence of mechanical modes

Figure 5 – Dispersion relation bandgap in a phononic crystal

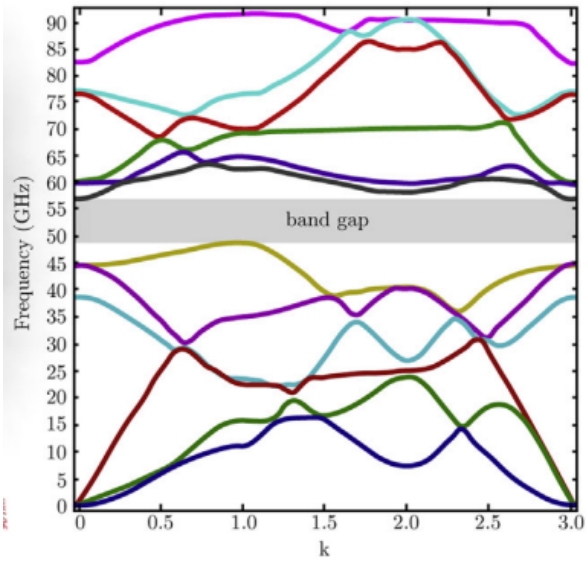

Source: J.N. Becker (2017) [13]

allows one to tune the heat conductivity of a (matrix) material that is a good conductor into a heat insulator, only by modifying the type and the periodicity of defects inserted into it.

The key factors for the appearance of this zone folding behaviour on the dispersion relations seems to be the difference in the velocity of sound, elastic constants and density between the matrix and the defect material [14].

Our goal with this work is to explore these periodic array of defects with different geometrical shapes in Si membranes and see how they can affect its heat conductivity. For thermal conductivity calculations we will be using molecular dynamics and a method called Homogeneous Non Equilibrium Molecular Dynamics (HNEMD), which will be further detailed in chapter 3, section 3.2. Before getting into the methodology section we will detail, in the next chapter 2, another approach to calculate heat conductivity which is the one of solving the Boltzmann Transport Equation (BTE).

2 HEAT CONDUCTIVITY THEORY

The state of the art approaches of solving the BTE equation usually rely on approximation of three, four and higher order phonon scattering process that usually rely on first principle calculations [20, 21]. Despite using this method not being the focus of our work here, a simpler approximation of the BTE can be explored to offer some insight into how each individual phonon branch contributes to the overall thermal conductivity. In order to write an expression for the transport coefficients associated with phonons (heat conductivity coefficient) in terms of microscopic variables, it is necessary to solve the BTE. The derivation of the equations in the next sections will be based on Henry [22] and Ziman's book [23, Chapter 7].

2.1 BOLTZMANN TRANSPORT EQUATION

The BTE is an equation that relates the scattering rates of microscopic particles (electrons and phonons) with the forces acting upon them. The function that represents the particles is the probability distribution function $f(r)$, and it represents the number of particles in the neighborhood of r, in essence the occupation number. At equilibrium, when no perturbations are applied to the system this function f^0 has the form for phonons (for electrons) of the Bose-Einstein (Fermi-Dirac) distribution:

$$f^0 = \frac{1}{e^{\frac{(E-\mu)}{k_B T}} + \eta} \tag{2.1}$$

where h is planck's constant, k_B is Boltzmann constant, T is the temperature, E is the system energy and μ is the chemical potential. Also $\eta = +1$ for electrons and $\eta = -1$ for phonons. For phonons we can take $E = h\nu$, where ν is the phonon frequency.

Working in k-space the function $f(r)$ depends on the crystal momentum of the lattice so it will be relabeled as f_k, and with this notation the full BTE, under the assumption of steady state condition, can be written as:

$$\dot{f}_k(\text{diffusion}) + \dot{f}_k(\text{fields}) + \dot{f}_k(\text{scattering}) = 0, \tag{2.2}$$

the first term on the left hand side is related to diffusion. Using the chain rule, the probability distribution f_k changes with time as:

$$\dot{f}_k(\text{diffusion}) = -\frac{\partial f_k}{\partial \mathbf{r}}.\frac{\partial \mathbf{r}}{\partial t} = -\mathbf{v}_k.\frac{\partial f_k}{\partial \mathbf{r}}, \tag{2.3}$$

the second term is related to how external fields are able to change the distribution f, as before the chain rule gives:

$$\dot{f}_k(\text{fields}) = -\frac{\partial f_k}{\partial \mathbf{k}}.\frac{\partial \mathbf{k}}{\partial t}, \tag{2.4}$$

for phonons the term $\frac{\partial \mathbf{k}}{\partial t} = 0$, but for carriers with charge (electrons or holes), the term $\dot{\mathbf{k}}$ can be written as:

$$\begin{aligned} \dot{\mathbf{k}} &= \frac{e}{\hbar}\left[\mathbf{E} + (\mathbf{v}_k \times \mathbf{B})\right] \\ \dot{f}_k(\text{fields}) &= -\frac{\partial f_k}{\partial \mathbf{k}}.\left(\frac{e}{\hbar}\left[\mathbf{E} + (\mathbf{v}_k \times \mathbf{B})\right]\right) \end{aligned} \tag{2.5}$$

where $\mathbf{E}$ and $\mathbf{B}$ are the external electric and magnetic field, respectively. And e represents the elementary electron's charge, such that $e < 0$ for an electron and $e > 0$ for a hole. Substituting equations 2.3, 2.4 and 2.5 back into 2.2 we get the full BTE equation:

$$\dot{f}_k(\text{scattering}) = \mathbf{v}_k.\frac{\partial f_k}{\partial \mathbf{r}} + \frac{\partial f_k}{\partial \mathbf{k}}.\left(\frac{e}{\hbar}\left[\mathbf{E} + (\mathbf{v}_k \times \mathbf{B})\right]\right) \tag{2.6}$$

2.2 LINEARIZED BOLTZMANN EQUATION SOLUTION FOR PHONONS

The whole problem of solving the BTE is the scattering term on the left hand side of equation 2.6. The simplest assumption is to consider that the probability distribution does not deviate much from its equilibrium form in equation 2.1 and since the condition $\dot{f}_k(\text{scattering})^0 = 0$ has to be satisfied, the scattering term can be written as:

$$\dot{f}_k(\text{scattering}) = -\frac{f_k - f_k^0}{\tau} \tag{2.7}$$

where f_k^0 is given in 2.1 and τ is a relaxation constant that holds information about scattering events, the minus sign is convention. Substituting that on the full BTE equation for phonons (where the second term on the right hand side in equation 2.6 is zero), we obtain the linearized Boltzmann equation:

$$f_k = f_k^0 - \left(\mathbf{v}_k.\frac{\partial f_k}{\partial \mathbf{r}}\right)\tau \tag{2.8}$$

from the form of f_k^0 one seems to think that the function f_k does not depend on the position, but if we assume once again the chain rule and the fact that f_k represents a small deviation from f_k^0, then:

$$\begin{aligned} \frac{\partial f_k}{\partial \mathbf{r}} &\approx \frac{\partial f_k^0}{\partial T}\nabla T \\ f_k &= f_k^0 - \left(\frac{\partial f_k^0}{\partial T}\mathbf{v}_k.\nabla T\right)\tau \end{aligned} \tag{2.9}$$

where ∇T represents the temperature gradient on the system. Equation 2.9 is the Linearized Boltzmann equation for phonons. Once the solution is found, one can calculate the heat flux along any specific direction $\hat{\mathbf{x}}$ of the system as:

$$J(x) = \frac{1}{V}\sum_{\lambda}\sum_{k} E_{k,\lambda}.f_{k,\lambda}.\mathbf{v}_{k,\lambda}.\hat{\mathbf{x}} \tag{2.10}$$

where λ represents the polarization of the mode, k the sum over reciprocal space, and V is the sample volume. The sum over k-space can be converted into an integral and we can assume that the density of states as a function of k possess spherical symmetry (the last assumption will be drooped latter on):

$$\begin{aligned} \sum_k &\rightarrow \int d^3k \\ d^3k &= \frac{k^2 dk d\Omega}{\left(\frac{2\pi}{a}\right)^3} \end{aligned} \tag{2.11}$$

where the variable a represents the separation distance between the atoms. With those two assumptions the heat flux can be rewritten as:

$$\begin{aligned} J(x) &= \frac{1}{V}\sum_{\lambda}\int_{k=0}^{k=\infty}\int_{\Omega} E_{k,\lambda}.f_{k,\lambda}.v_{x,\lambda}\frac{k^2 dk d\Omega}{\left(\frac{2\pi}{a}\right)^3} \\ J(x) &= \frac{1}{V}\sum_{\lambda}\int_0^{\infty} E_{k,\lambda}.f_{k,\lambda}.v_{x,\lambda}.D(k)dk \end{aligned} \tag{2.12}$$

where on the last line of eq. 2.12 the condition of phase space spherical symmetry was drooped. This can be seen by noticing that:

$$D(k)dk = \int_{\Omega}\frac{k^2 dk d\Omega}{\left(\frac{2\pi}{a}\right)^3} \tag{2.13}$$

where $D(k)dk$ represents the density of states in terms of wave vector k. In the density of states definition $D(k)dk = D(\nu)d\nu = D(E)dE$, such that the integral over k may be changed into an integral over frequency, up to some frequency ν_{max}. And using the fact that $E_k = h\nu$ we obtain:

$$J(x) = \frac{1}{V}\sum_{\lambda}\int_{0}^{\nu_{max}} h\nu_{\lambda}.f_{k,\lambda}.v_{x,\lambda}.D(\nu)d\nu_{\lambda} \tag{2.14}$$

where at equilibrium there is no average heat flux, such that the integral in 2.14 for f_k^0 vanishes. Then substituting the last line in eq. 2.9 on the previous integral, we get:

$$J(x) = -\frac{1}{V}\sum_{\lambda}\int_{0}^{\nu_{max}} h\nu_{\lambda}.\frac{\partial f_k^0}{\partial T}v_{x,\lambda}^2.\tau_{\lambda}.\frac{\partial T}{\partial x}D(\nu)d\nu_{\lambda} \tag{2.15}$$

where if the system is isotropic, $v_x^2 = \frac{1}{3}v^2$. We can also define the heat capacity per unit volume as a function of frequency as $C(\nu) = \frac{1}{V}\left(h\nu\frac{\partial f_k^0}{\partial T}D(\nu)\right)$, so the heat flux can be rewritten as:

$$J(x) = -\frac{1}{3}\sum_{\lambda}\int_{0}^{\nu_{max}} C_{\lambda}(\nu)v_{\lambda}^2.\tau_{\lambda}.d\nu_{\lambda}.\frac{\partial T}{\partial x} \tag{2.16}$$

this expression has the same form as the Fourier equation $J = -\kappa\nabla T$ with heat conductivity κ being given by:

$$\kappa = -\frac{1}{3}\sum_{\lambda}\int_{0}^{\nu_{max}} C_{\lambda}(\nu)v_{\lambda}^2.\tau_{\lambda}.d\nu_{\lambda}, \tag{2.17}$$

and in general C_λ, v_λ and τ_λ depend on the phonon branch λ being considered. By using the definiton of mean free path $\Lambda = v\tau$, eq. 2.17 can be rewritten as:

$$\kappa = -\frac{1}{3}\sum_{\lambda}\int_{0}^{\nu_{max}} C_{\lambda}(\nu)v_{\lambda}.\Lambda_{\lambda}.d\nu \tag{2.18}$$

that is, the overall thermal conductivity relates to the modal heat capacity, group velocity and mean free path of each phonon mode.

3 METHODOLOGY

3.1 MOLECULAR DYNAMICS SIMULATION

Molecular Dynamics (MD) is a simulation method that allows one to obtain time evolution for atomic systems, and as consequence calculate quantities that exhibit time variation. This kind of simulation is used in a large range of areas going from biology [24], to chemistry [25, 26] and even condensed matter physics [27, 28]. Trajectories are generated following the laws of classical mechanics. For the simplest formalism, keeping the number of particles constant, the volume of the interest region fixed and requiring conservation of energy, we obtain the NVE ensemble. Under NVE conditions, Hamilton equations reduce to the Newtonian equations of motion. Given a potential function V, for a particle of mass m and velocity v the Newtonian equations of motion goes as follows:

$$\begin{aligned} \boldsymbol{F_i} &= -\nabla_i V \\ \ddot{\boldsymbol{q}}_{\boldsymbol{i}} &= \frac{\boldsymbol{F_i}}{m_i} \\ \dot{\boldsymbol{q}}_{\boldsymbol{i}} &= \boldsymbol{v_i} \end{aligned} \tag{3.1}$$

These equations can be numerically integrated to obtain the positions $\boldsymbol{q}_i(t)$ and velocities $\dot{\boldsymbol{q}}_i(t)$ for all particles i in the system, given the necessary initial conditions (starting geometry and initial velocities of all particles). Newtonian equations can be numerically integrated to obtain the trajectories of each particle on the system. Different numerical methods can be used to integrate these equations of motion. The simplest method for integration of differential equations in general is to assume that the derivative can be approximated by a ratio, if dt is sufficiently small, that results in what is called the Euler method [29]:

$$\begin{aligned} \frac{\boldsymbol{q}_i(t+dt) - \boldsymbol{q}_i(t)}{dt} &\approx \dot{\boldsymbol{q}}_i(t) \\ \boldsymbol{q}_i(t+dt) &\approx \boldsymbol{q}_i(t) + \boldsymbol{v}_i dt \\ \boldsymbol{v}_i(t+dt) \approx \boldsymbol{v}_i(t) + \ddot{\boldsymbol{q}}_i(t)dt &= \boldsymbol{v}_i(t) + \frac{\boldsymbol{F}_i}{m_i}dt \end{aligned} \tag{3.2}$$

The Euler method is just a Taylor series expansion for $\boldsymbol{q}_i(t)$ and $\boldsymbol{v}_i(t)$ truncated at first order. The global error in Euler method is of order $O(dt)$, that is, it scales linearly with dt. Even if a relatively small dt is chosen, accumulation of error makes the solutions for $\boldsymbol{q}_i(t)$ and

$\boldsymbol{v}_i(t)$ diverge if a large number of iterations is required, which results in non conservation of energy. For that reason, the Euler method is rarely used for time integration in MD simulations.

Another method of integration is the Verlet algorithm [30, Chapter 3]. If we write the Taylor series expansion for $\boldsymbol{q}_i(t+dt)$ and $\boldsymbol{q}_i(t-dt)$, we have:

$$\begin{aligned} \boldsymbol{q}_i(t+dt) &= \boldsymbol{q}_i(t) + \boldsymbol{v}_i(t)dt + \frac{1}{2}\boldsymbol{a}_i(t)dt^2 \\ \boldsymbol{q}_i(t-dt) &= \boldsymbol{q}_i(t) - \boldsymbol{v}_i(t)dt + \frac{1}{2}\boldsymbol{a}_i(t)dt^2 \end{aligned} \tag{3.3}$$

Summing both equations in 3.3 we get the final form of the Verlet algorithm:

$$\boldsymbol{q}_i(t+dt) = 2\boldsymbol{q}_i(t) - \boldsymbol{q}_i(t-dt) + \boldsymbol{a}_i(t)dt^2 \tag{3.4}$$

Note that as velocity cancelled, if we had expanded the Taylor series up to third order in 3.3, the terms carrying dt^3 would also cancel (in fact, all of the odd terms would cancel). So, the local error on Verlet algorithm is of order $O(dt^4)$. This makes the Verlet algorithm much more precise than the previous presented Euler method. Then, the original Verlet algorithm does not require information about velocities, but it is necessary to have information about $\boldsymbol{q}_i(t-dt)$ and $\boldsymbol{q}_i(t)$ to initiate the method. A common way of circumvent this problem is to use the initial positions as $\boldsymbol{q}_i(0)$ and calculate $\boldsymbol{q}_i(1)$ as in the Euler method. Then, from $\boldsymbol{q}_i(2)$ onward, use equation 3.4. If velocities are required, it is possible to use the mid point rule to calculate $\boldsymbol{v}_i(t)$ as a ratio between $\boldsymbol{q}_i(t+dt)$ and $\boldsymbol{q}_i(t-dt)$:

$$\boldsymbol{v}_i(t) \approx \frac{\boldsymbol{q}_i(t+dt) - \boldsymbol{q}_i(t-dt)}{2dt} \tag{3.5}$$

Large-scale Atomic Molecular Massively Parallel Simulator (LAMMPS) use a variation of the Verlet algorithm to integrate the differential equations under NVE conditions, which is called Stormer-Verlet Algorithm or velocity-Verlet [30, Chapter 3]. The algorithm is similar, but the step by step calculation of positions now depend on velocity. And the velocity calculation depend on an average between $\boldsymbol{a}_i(t)$ and $\boldsymbol{a}_i(t+dt)$:

$$\begin{aligned} \boldsymbol{q}_i(t+dt) &= \boldsymbol{q}_i(t) + \boldsymbol{v}_i(t)dt + \frac{1}{2}\boldsymbol{a}_i(t)dt^2 \\ \boldsymbol{v}_i(t+dt) &= \boldsymbol{v}_i(t) + \frac{1}{2}\left[\boldsymbol{a}_i(t+dt) + \boldsymbol{a}_i(t)\right] \end{aligned} \tag{3.6}$$

The advantage of using 3.6 over 3.4 and 3.5 is that, for the velocity-Verlet, the algorithm is self initiative. That is, given the set of initial positions $\boldsymbol{q}_i(0)$ and velocities $\boldsymbol{v}_i(0)$, all of the subsequent steps can be directly calculated from the set of equations 3.6. The local error is the

same as in the original Verlet method, $O(dt^4)$. The step by step sequence to update positions and velocities under this algorithm would be:

1. calculate acceleration $\boldsymbol{a}_i(0)$ based on initial positions $\boldsymbol{q}_i(0)$
2. calculate $\boldsymbol{q}_i(dt)$, using the first equation in 3.6
3. calculate $\boldsymbol{a}_i(dt)$ based on the new positions $\boldsymbol{q}_i(dt)$
4. calculate $\boldsymbol{v}_i(dt)$ using the equation for velocities in 3.6
   And iterate the steps $2-4$ up to the final timestep:
5. calculate $\boldsymbol{q}_i(2dt)$, using the first equation in 3.6
   $\vdots$

Note that in all of our previous discussions, it was always required to calculate the acceleration at a given timestep t. That is where it lies the heart of MD simulations. The calculation of acceleration is directly related to the force field, as given in equation 3.1. The results obtained by the simulation are only reliable if the potential given by the force field is a good representative of the system being simulated. For calculation of mechanical properties involving Si, the Tersoff's Potential [31, 32] remains the optimal choice, when it comes to empirically parametrized potentials.

3.1.1 Tersoff's Potential

The Tersoff potential was originally parametrized to reproduce lattice parameter and elastic constants of bulk silicon [31]. The potential energy is written as a sum of cohesive energies over each lattice site, in which the energy of a site is given by the interaction of an atom at site i with all of its nearest neighbors j:

$$E = \sum_i E_i = \sum_{i \neq j} \frac{1}{2} V_{ij} \tag{3.7}$$

Despite looking like a two-body potential function, that is not the case. The interaction energy V_{ij} for a given pair of atoms i, j also depends on the interaction between atom i and all of its other nearest neighbors k, for $k \neq j$. That is, for the Tersoff model, the bonding between two atoms i, k can indirectly strengthen or weaken the ij bond, depending on their relative

distances and angles. This characterizes V_{ij} as a many-body potential, with the functional form:

$$
\begin{aligned}
V_{ij} &= f_C(r_{ij})[f_R(r_{ij}) + b_{ij} f_A(r_{ij})]; \\
f_R(r) &= Aexp(-\lambda r); \\
f_A(r) &= -Bexp(-\mu r); \\
f_C(r_{ij}) &= \begin{cases} 1, & r_{ij} < R \\ \frac{1}{2}\left(1 + cos[\pi \frac{(r_{ij}-R)}{S-R}]\right), & R < r_{ij} < S \\ 0, & r_{ij} > S \end{cases} \\
b_{ij} &= (1 + \beta_i^{n_i} \zeta_{ij}^{n_i})^{-\frac{1}{2n_i}} \\
\zeta_{ij} &= \sum_{k \neq i,j} f_C(r_{ik}) g(\theta_{ijk}) \\
g(\theta_{ijk}) &= \gamma_{ijk} \left(1 + \frac{c_i^2}{d_i^2} - \frac{c_i^2}{[d_i^2 + (h_i - cos\theta_{ijk})^2]}\right)
\end{aligned}
\tag{3.8}
$$

where f_R is a repulsive term, f_A is an attractive term, f_C is a smooth cutoff function, that goes from 1 to 0, chosen to guarantee continuity of the derivatives. ζ_{ij} is the term that contains the influence of the ik bonds with nearest neighbors over the ij bond. θ_{ijk} represents the angle between the ij bond and the ik bond. The parameter c_i represents the intensity of the angular effect and d_i its "sharpness", that is, if d_i is large (small) the angular variations would affect less (more) the value of $g(\theta_{ijk})$. h_i represents the $cos(\theta_0)$ with θ_0 representing the equilibrium angle between the ij and ik bonds.

Despite being originally parameterized to represent lattice and elastic constants, Tersoff showed on its first paper [31] that phonon dispersion relations calculated through lattice dynamics for bulk Si were in good agreement with experimental data, even though no phonon parameter was used to fit the potential.

The highest discrepancies are found near the first BZ boundaries for the acoustic phonons. Since 1989, several other attempts have been made to parameterize potentials for bulk silicon. As we can see in Fan's paper Fig.4 [33] reprinted here in Fig. 6, most of the empirical potentials developed so far (including his modified version called mini-Tersoff), have trouble near the zone boundary matching the experimental results for some of the acoustic branches. This certainly has an effect on thermal conductivity.

Fan showed that his mini-Tersoff potential has a better agreement than Tersoff itself to thermal conductivity of bulk silicon at various temperatures (including $T = 300$ K). No silicon

Figure 6 – Reprinted phonon dispersion relations for bulk diamond silicon for different MD potential energy functions, including the original Tersoff potential. Red line represents empirical potentials results and blue dots represents experimental results.

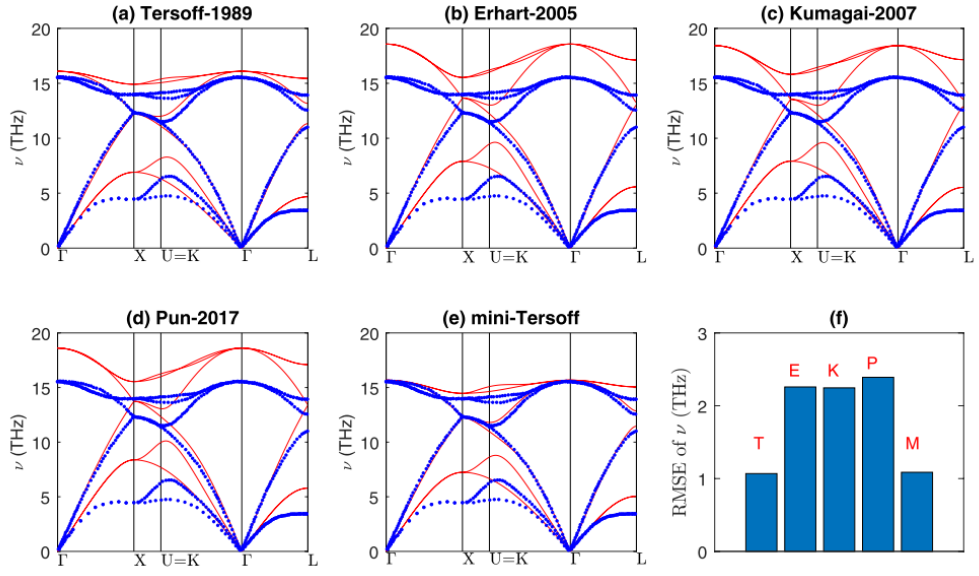

Source: Fan et. al [33] (2019)

membranes have been tested in his work. Neogi and Donadio [11] have recently tried to compute heat conductivity for silicon membranes using Tersoff's potential, but the authors claimed that their results do not seem to quantitativaly agree with experiments.

Henry [22] used Enviroment-Dependent Interatomic Potential (EDIP) [34] to calculate thermal conductivity of bulk silicon as a function of temperature and his results seem to be comparable, when it comes to agreement with experiments, as the ones obtained by Fan. Although EDIP is computationally more expensive due to a higher number of parameters when compared to Tersoff and specially mini-Tersoff which has 3 parameters less than Tersoff.

Throughout all of this work we used only Tersoff 1989 [32] potential, which in terms of empirical potentials is one of the simplest and more computationally efficient potentials. It was designed to represent bulk silicon we assume will also work well for Si membranes.

3.1.2 Thermostats

If simulations out of the microcanonical (NVE) ensemble are required, as NVT or NPT, for example, there needs to be a way of controlling the system's temperature or pressure as we integrate the equations of motion during the production run. Controlling the temperature during the simulation is the role of thermostats.

3.1.2.1 Berendsen

One of the simplest algorithms to couple the system temperature to a heat bath is the Berendsen Thermostat. Berendsen [35] started with the idea of modifying the equations of motion inserting a friction term γ (chosen to be equal for all particles, for simplicity) on the system and a random noise $\boldsymbol{R_i}(t)$, which results in a Langevin equation:

$$m_i \dot{\boldsymbol{v}}_{\boldsymbol{i}} = \boldsymbol{F_i} - m_i \gamma \boldsymbol{v_i} + \boldsymbol{R_i}(t) \tag{3.9}$$

where the random noise vector $\boldsymbol{R_i(t)}$ shows a delta time correlation function of the form:

$$\int_0^\infty \boldsymbol{R_i}(t)\boldsymbol{R_j}(t+\tau)dt = 2m_i\gamma k_B T_0 \delta(\tau)\delta_{ij} \tag{3.10}$$

where i and j stands for the particle's index. This procedure allows to weak couple the system's degrees of freedom with an external reservoir at a temperature T_0. In order to derive an expression for the equation of motion for the temperature of the bath at all times t is helpful to evaluate the time derivative of kinetic energy for the system:

$$\frac{\mathrm{d}E_{kin}}{\mathrm{d}t} = \lim_{\Delta t \to 0} \left[\frac{\sum_{k=1}^{3N} \frac{m_k}{2} \left(v_k^2(t+\Delta t) - v_k^2(t)\right)}{\Delta t} \right], \tag{3.11}$$

where N represents the number of particles, k goes from 1 to $3N$ degrees of freedom. Integration of equation 3.9 from time t to $t+\Delta t$ allows to obtain the difference Δv:

$$\begin{aligned} \Delta v_k &= v_k(t+\Delta t) - v_k(t) \\ \Delta v_k &= \frac{1}{m_k} \int_t^{t+\Delta t} F_k(t') + m_k \gamma v_k(t') + R_k(t') dt' \end{aligned} \tag{3.12}$$

From the first equation of 3.12, we can obtain the relation:

$$v_k^2(t+\Delta t) - v_k^2(t) = {\Delta v_k}^2 + 2\Delta v_k v_k(t) \tag{3.13}$$

Substituting 3.13 and the second equation of 3.12 in 3.11, and using the result for the correlation for $\boldsymbol{R_i}(t)$ in 3.10 we end up with:

$$\begin{aligned} \frac{\mathrm{d}E_{kin}}{\mathrm{d}t} &= \lim_{\Delta t \to 0} \left[\frac{\sum_{k=1}^{3N} (F_k v_k + \gamma k_B T_0 - m_k \gamma v_k^2)\Delta t + O(\Delta t^2)}{\Delta t} \right] \\ \frac{\mathrm{d}E_{kin}}{\mathrm{d}t} &= \sum_{k=1}^{3N} F_k v_k + \gamma(3Nk_B T_0 - 2E_{kin}) \\ \frac{\mathrm{d}E_{kin}}{\mathrm{d}t} &= \sum_{k=1}^{3N} F_k v_k + 2\gamma(\frac{3}{2}Nk_B T_0 - E_{kin}) \end{aligned} \tag{3.14}$$

where the second term on the right-hand side (written in terms of temperature) represents the equation for the time evolution of the reservoir temperature:

$$\left(\frac{\mathrm{d}T}{\mathrm{d}t}\right)_{reservoir} = 2\gamma(T_0 - T) \tag{3.15}$$

choosing $\boldsymbol{R_i}(t) = m_i\gamma\frac{T}{T_0}\boldsymbol{v_i}$ makes the time derivative of the kinetic energy exactly equal to that obtained in the last equation 3.14. Note that the noise has no explicit dependence on time. Although he started the derivation with the hypothesis that the equation had a stochastic term $\boldsymbol{R_i}(t)$ in it, this term did not need to be stochastic to fulfill the requirement of coupling the system to a bath. Which results in the final equation of motion:

$$m_i\dot{\boldsymbol{v}}_{\boldsymbol{i}} = \boldsymbol{F_i} + m_i\gamma\left(\frac{T_0}{T} - 1\right)\boldsymbol{v_i} \tag{3.16}$$

So the whole Berendsen method is equivalent to the transformation $\boldsymbol{v_i} \to \lambda\boldsymbol{v_i}$, with λ equal to: (with $\gamma = \frac{1}{2\tau}$)

$$\lambda = \left[1 + \frac{\Delta t}{2\tau}\left(\frac{T_0}{T} - 1\right)\right] \tag{3.17}$$

The Berendsen method fails to reproduce phase space trajectories for the canonical ensemble, producing unrealistic fluctuations [36] and can only be used for equilibration of temperature, not for full canonical NVT simulations.

3.1.2.2 Nosé-Hoover and the Chains

The Nosé-Hoover thermostat comes to solve the problem of non-canonical phase space trajectories that happened in the Berendsen thermostat. To derive his equations of motion, Nosé [37] used the strategy of re-scaling time by the transformation:

$$dt' = \frac{dt}{s} \tag{3.18}$$

The variable s represents the degree of freedom associated with the thermostat. With this scaling procedure, momentum and positions (real variables) are transformed into what he called "virtual variables":

$$\begin{aligned} \boldsymbol{p_i}' &= \frac{\boldsymbol{p_i}}{s} \\ \boldsymbol{q_i}' &= \boldsymbol{q_i} \end{aligned} \tag{3.19}$$

where $\boldsymbol{p_i}'$ and $\boldsymbol{q_i}'$ are the real momentum and position of the particle i, respectively. The set $\{\boldsymbol{p_i}, \boldsymbol{q_i}\}$ represents the set of virtual momentum and position of all particles i in the system, respectively. With this transformation, the following hamiltonian can be written as:

$$H(\boldsymbol{q_i}, \boldsymbol{p_i}, p_s, s) = \sum_{i=1} \frac{\boldsymbol{p_i}.\boldsymbol{p_i}}{2m_i s^2} + \phi(\boldsymbol{q_i}) + \frac{p_s^2}{2Q} + (N_{df}+1)k_B T ln(s) \tag{3.20}$$

where N_{df} represents the number of the system's degrees of freedom, p_s represents the momentum associated with the variable s and the parameter Q is a fictitious mass term for the thermostat which represents the strength of the coupling between the system and the reservoir.

From 3.20 the equations of motion based on virtual variables were found to be (i=1,2,...,N):

$$\begin{aligned}
\dot{\boldsymbol{q}}_{\boldsymbol{i}} &= \frac{\mathrm{d}H}{\mathrm{d}\boldsymbol{p_i}} = \frac{\boldsymbol{p_i}}{m_i s^2} \\
\dot{\boldsymbol{p}}_{\boldsymbol{i}} &= -\frac{\mathrm{d}H}{\mathrm{d}\boldsymbol{q_i}} = \boldsymbol{F_i}(\{\boldsymbol{q_i}\}) \\
\dot{s} &= \frac{\mathrm{d}H}{\mathrm{d}p_s} = \frac{p_s}{Q} \\
\dot{p_s} &= -\frac{\mathrm{d}H}{\mathrm{d}s} = \sum_i \frac{\boldsymbol{p_i}.\boldsymbol{p_i}}{m_i s^3} - \frac{(N_{df}+1)\,k_B T}{s}
\end{aligned} \tag{3.21}$$

Nosé showed that this set of equations generates an ensemble that is compatible with the canonical distribution. The only inconvenience was that these equations were only canonical under this "virtual variable" form. Only one year later, Hoover [38] showed that writing equations 3.21 back in terms of real variables, with the definition of $\zeta = \dot{s}$, leads to:

$$\begin{aligned}
&\dot{\boldsymbol{q}}_i = \frac{\boldsymbol{p}_i}{m_i s^2} = \frac{\boldsymbol{p}_i'}{m_i s} \rightarrow \frac{\mathrm{d}\boldsymbol{q'}}{\mathrm{d}t'} = \frac{\boldsymbol{p_i'}}{m_i} \\
&\dot{\boldsymbol{p}}_i = \frac{\mathrm{d}\,(\boldsymbol{p}_i' s)}{\mathrm{d}t} = \frac{\mathrm{d}\boldsymbol{p}_i'}{\mathrm{d}t} s + \boldsymbol{p}_i' \frac{\mathrm{d}s}{\mathrm{d}t} = \boldsymbol{F}(\{\boldsymbol{q}_i\}) \rightarrow \frac{\mathrm{d}\boldsymbol{p}_i'}{\mathrm{d}t'} = \boldsymbol{F}(\{\boldsymbol{q}_i'\}) - \zeta \boldsymbol{p}_i' \\
&\dot{\zeta} = \frac{1}{Q}\dot{p_s} = \frac{1}{Q}\left[\sum_i \frac{\boldsymbol{p}_i.\boldsymbol{p}_i}{m_i s^3} - \frac{(N_{df}+1)kT}{s}\right] = \frac{1}{Q}\left[\sum_i \frac{\boldsymbol{p}_i'.\boldsymbol{p}_i'}{m_i s} - \frac{(N_{df}+1)k_B T}{s}\right] \\
&\rightarrow \frac{\mathrm{d}\zeta}{\mathrm{d}t'} = \frac{1}{Q}\left[\sum_i \frac{\boldsymbol{p}_i'.\boldsymbol{p}_i'}{m_i} - (N_{df}+1)k_B T\right]
\end{aligned} \tag{3.22}$$

It has also been showed by Hoover on the same paper, that the transformation $(N_{df}+1) \rightarrow N_{df}$ makes the set of simultaneous equations (i=1,2,...,N),

$$\begin{aligned}
\frac{\mathrm{d}\boldsymbol{q'}}{\mathrm{d}t'} &= \frac{\boldsymbol{p_i'}}{m_i} \\
\frac{\mathrm{d}\boldsymbol{p_i'}}{\mathrm{d}t'} &= \boldsymbol{F_i}(\{\boldsymbol{q_i'}\}) - \zeta \boldsymbol{p_i'} \\
\frac{\mathrm{d}\zeta}{\mathrm{d}t'} &= \frac{1}{Q}\left[\sum_i \frac{\boldsymbol{p_i'}.\boldsymbol{p_i'}}{m_i} - N_{df} k_B T\right]
\end{aligned} \tag{3.23}$$

dependent only on the set of real variables $\{\boldsymbol{q}'_i, \boldsymbol{p}'_i, \zeta\}$, obey the canonical distribution. Clearly from the second equation in 3.23 the ζ parameter works as a friction term, that slows down the particles, in order to keep constant the system's average temperature.

Despite the probability distribution on the variables, $\boldsymbol{q}'_i, \boldsymbol{p}'_i$ and ζ satisfying the canonical distribution, Hoover [38] applied the equations 3.23 for a one dimensional harmonic oscillator and the trajectories obtained did not seem to fill the whole phase space. If the trajectories are not chaotic (fill the whole phase space), ergodicity can not be applied to the system. If the system is not ergodic, then time averages are not good representatives of ensemble averages and the usual thermodynamic quantities can not be computed via MD simulations.

To solve the problem of ergodicit, Martyna *et. al* [39] proposed a modification on the Hoover equations of motion in order to include more than one thermostat variable:

$$\begin{aligned}
\dot{\boldsymbol{q}}_i &= \frac{\boldsymbol{p}_i}{m_i} \\
\dot{\boldsymbol{p}}_i &= -\frac{\partial V}{\partial \boldsymbol{q}_i} - \boldsymbol{p}_i \frac{p_{\eta_1}}{Q_1} \\
\dot{\eta_j} &= \frac{p_{\eta_j}}{Q_j} \\
\dot{p_{\eta_1}} &= \left[\sum_i \frac{p_i^2}{m_i} - N_{df} k_B T\right] - p_{\eta_1} \frac{p_{\eta_2}}{Q_2} \\
\dot{p_{\eta_j}} &= \left[\frac{p_{\eta_{j-1}}^2}{Q_{j-1}} - k_B T\right] - p_{\eta_j} \frac{p_{\eta_{j+1}}}{Q_{j+1}} \\
\dot{p_{\eta_M}} &= \left[\frac{p_{\eta_{M-1}}^2}{Q_{M-1}} - k_B T\right]
\end{aligned} \tag{3.24}$$

where M is the number of additional thermostats added. The variable $\dot{\eta_1}$ is exactly the same as ζ defined in the Hoover equations, and p_{η_j} is the momentum associated with the extra thermostat variable j.

In fact, a linear chain of thermostats are added, where only the first thermostat is in contact with the whole N_{df} degrees of freedom of the system, and after the first, the other $\dot{p_{\eta_j}}$ variables for $j > 1$ are only in contact with its first neighbors. That is why this algorithm is also called, Nosé-Hoover chain algorithm.

3.1.2.3 Langevin

The Langevin equation is the same used at the starting point of the derivation for the Berendsen method 3.9. The difference lies in the random force term $\boldsymbol{R_i}(t)$. In the original

Langevin equations $\boldsymbol{R_i}(t)$ is a random force term that acts every time step, following a Gaussian distribution, with zero mean and delta function correlation given by 3.10. As Schneider [40] showed (appendix A on his paper) the random force term has the functional form:

$$R_i^\alpha(t) = \left(\frac{2mk_BT\gamma\Delta}{p}\right)^{1/2} \sum_j \delta(t-t_j)\beta_i^\alpha(t_j)\Theta(p-a_{0ij}^\alpha) \tag{3.25}$$

where α represents a component of the vector, Δ represents a time step, j counts the timesteps, β_i^α and a_{0ij}^α are random numbers between 0 and 1 that follow a Gaussian and a uniform distribution, respectively. The Heavside function $\Theta(p-a_{0ij}^\alpha)$ associated with the parameter p, means that the random process only takes place if the random number a_{0ij}^α is greater than the probability p associated with the collision.

This would be the form of the random force vector if the equation 3.9 was a continuous function. As the goal is to perform MD simulations on it, where the equations will be integrated numerically, it needs some adjustments. But before that, the delta function in 3.25 implies a discontinuity at the velocities, that can be found by integrating 3.9 from $t_j+\epsilon$ and $t_j-\epsilon$ and then taking the limit $\epsilon \to 0$:

$$\int_{t_j-\epsilon}^{t_j+\epsilon} \dot{v_i}^\alpha(t')dt' = \int_{t_j-\epsilon}^{t_j+\epsilon} \frac{1}{m_i}R_i^\alpha(t')dt' + \int_{t_j-\epsilon}^{t_j+\epsilon} \frac{1}{m_i}F_i^\alpha dt' + \int_{t_j-\epsilon}^{t_j+\epsilon} \frac{1}{m_i}v_i^\alpha(t')dt' \tag{3.26}$$

the integral on F_i vanishes in the limit that ϵ goes to zero because the force is continuous, and the integral on $v_i(t')$ also goes to zero, due to continuity of $x_i^\alpha(t_j)$. Then we end up with:

$$\begin{aligned} &\int_{t_j-\epsilon}^{t_j+\epsilon} \dot{v_i}^\alpha(t')dt' = \int_{t_j-\epsilon}^{t_j+\epsilon} \frac{1}{m_i}R_i^\alpha(t')dt' \\ &v_i^\alpha(t_j+0^+) - v_i^\alpha(t_j-0^-) = \left(\frac{2k_BT\gamma\Delta}{m_ip}\right)^{1/2} \beta_i^\alpha(t_j)\Theta(p-a_{0ij}^\alpha) \end{aligned} \tag{3.27}$$

This gives the discontinuity of v_i^α at a time step t_j. From the form of equation 3.9 it can be seen that $v_i^\alpha(t) \sim e^{-\gamma t}$, or that $\dot{v_i^\alpha}(t) \sim -\gamma e^{-\gamma t}$ due to the friction term. With this assumption:

$$\int_0^\Delta v_i^\alpha(t)dt \sim \frac{1-e^{-\gamma\Delta}}{\gamma} \tag{3.28}$$

For small Δ :

$$\begin{aligned} \frac{1-e^{-\gamma\Delta}}{\gamma} &= \frac{1-e^{-\frac{\gamma\Delta}{2}}e^{-\frac{\gamma\Delta}{2}}}{\gamma} \\ &\approx \frac{1-e^{-\frac{\gamma\Delta}{2}}(1-\frac{\gamma\Delta}{2})}{\gamma} \\ &\approx \frac{\Delta}{2}e^{-\frac{\gamma\Delta}{2}} \end{aligned} \tag{3.29}$$

That is, the discontinuity on velocity in equation 3.27 implies a shift in position x_i^α at a time $t + \Delta$ of:

$$x_i^\alpha(t+\Delta) \sim \frac{\Delta}{2} e^{-\frac{\gamma\Delta}{2}} \left(\frac{2k_BT\gamma\Delta}{m_i p}\right)^{1/2} = \Delta^2 e^{-\frac{\gamma\Delta}{2}} \left(\frac{k_BT\gamma}{2m_i p\Delta}\right)^{1/2} \beta_i^\alpha \Theta(p - a_{0ii}^\alpha) \tag{3.30}$$

Now, the equation of motion 3.9 can not be integrated numerically using Verlet or velocity-verlet algorithm, because the acceleration is itself velocity dependent. To avoid this problem, Schneider [40] introduces a change of variables in the form:

$$\begin{aligned} x_i^\alpha(t) &= e^{-\frac{\gamma t}{2}} y_i^\alpha(t) \\ \dot{x_i}^\alpha(t) &= -\frac{\gamma}{2} e^{-\frac{\gamma t}{2}} y_i^\alpha + e^{\frac{-\gamma t}{2}} \dot{y_i}^\alpha \\ \ddot{x_i}^\alpha(t) &= \frac{\gamma^2}{4} e^{-\frac{\gamma t}{2}} y_i^\alpha - \gamma e^{-\frac{\gamma t}{2}} \dot{y_i}^\alpha + e^{-\frac{\gamma t}{2}} \ddot{y_i}^\alpha \end{aligned} \tag{3.31}$$

Substituting the set of equations in 3.31 on the original Langevin equation (eq. 3.9), without the random force term, we obtain an equation of motion in the new variable $y_i^\alpha(t)$, given by:

$$\ddot{y_i}^\alpha(t) = \frac{\gamma^2}{4} y_i^\alpha - \frac{1}{m_i} e^{\frac{\gamma t}{2}} (\nabla_i V)^\alpha \tag{3.32}$$

where V represents the potential energy function. Schneider chose to use Verlet integration on his implementation. So equation 3.32 can be integrated with Verlet scheme as:

$$\begin{aligned} \ddot{y_i}^\alpha(t) &= 2y_i^\alpha(t) - y_i^\alpha(t-dt) + dt^2 \ddot{y_i}^\alpha(t) \\ x_i^\alpha(t+dt) &= 2x_i^\alpha(t) e^{-\frac{\gamma dt}{2}} - e^{-\gamma dt} x_i^\alpha(t-dt) + dt^2 e^{-\frac{\gamma dt}{2}} \left(\frac{1}{4}\gamma^2 x_i^\alpha(t) - \frac{1}{m_i}(\nabla_i V)^\alpha\right) \end{aligned} \tag{3.33}$$

The second equation from 3.33 does not present translation invariance. So it can be converted to a more suitable form:

$$x_i^\alpha(t+dt) = x_i^\alpha(t) + \left[x_i^\alpha(t) - x_i(t-dt)\right] e^{-\gamma dt} - dt^2 e^{-\frac{\gamma dt}{2}} \frac{1}{m_i} (\nabla_i V)^\alpha \tag{3.34}$$

The equation above represents an algorithm for numerical integration of a differential equation that depends on velocity. But in equation 3.30, we saw that x_i^α is shifted (with a shift proportional to dt^2) due to the discontinuity imposed on $v_i^\alpha(t)$ due to the random force term. So equation 3.34 is modified to include this shift and becomes:

$$\begin{aligned} x_i^\alpha(t+dt) &= x_i^\alpha(t) + \left[x_i^\alpha(t) - x_i^\alpha(t-dt)\right] e^{-\gamma dt} \\ &- dt^2 e^{-\frac{\gamma dt}{2}} \frac{1}{m_i} \left[(\nabla_i V)^\alpha + \left(\frac{k_BT\gamma}{2m_i p dt}\right)^{1/2} \beta_i \Theta(p - a_{0ii})\right] \end{aligned} \tag{3.35}$$

This is the final form of the equation of motion in the algorithm of Schneider, in which the random force induces a change of trajectories which is proportional to $\left(\frac{k_B T \gamma}{m_i dt}\right)^{1/2}$. This samples canonical distribution of phase space, as long as $\gamma << f_s$ where f_s represents the natural frequency associated with the system.

3.1.2.4 BDP thermostat

Another thermostat that guarantees the canonical distribution is the one implemented by Bussi, Donadio and Parrinello [41]. Their thermostat is similar to the Berendsen 3.1.2.1, in the sense that it's also based on rescaling of a mechanical quantity associated with the dynamics, but instead of velocity, kinetic energy itself is rescaled. They argue on the paper that the choice of kinetic energy scaling is arbitrary, as long as it preservers the canonical distribution. With this in mind, their choice is to do time evolution on the kinetic energy, followed by stochastics dynamics. Their protocol for kinetic energy rescaling is: after time integration with an energy conserving algorithm (e.g. Velocity Verlet) to calculate velocities (and kinetic energies), the obtained values for kinetic energies are changed by the stochastic dynamics equation:

$$dK = (\bar{K} - K)\frac{dt}{\tau} + \sqrt{\frac{2K\bar{K}}{N_f \tau}}dW \tag{3.36}$$

where N_f is the number of degrees of freedom in the system, $\bar{K}$ is the target value for kinetic energy $\bar{K} = \frac{N_f}{2\beta}$ with $\beta = \frac{1}{k_B T}$. τ is the thermostat constant and dW is a random term called Wiener noise. If we take the random term $dW = 0$, the thermostat reduces to the one of Berendsen (eq. 3.16). To see that, putting K in evidence in 3.36:

$$\begin{aligned} dK &= \frac{K}{\tau}\left(\frac{\bar{K}}{K} - 1\right)dt \\ dK &= \frac{K}{\tau}\left(\frac{T_0}{T} - 1\right)dt \\ dK &= \sum_i \frac{m_i \boldsymbol{v}_i . \boldsymbol{v}_i}{2\tau}\left(\frac{T_0}{T} - 1\right)dt \end{aligned} \tag{3.37}$$

from the first to the second equation above the equipartition theorem for kinetic energy was used to set $\frac{\bar{K}}{K} = \frac{T_0}{T}$. And on the last equation the definition of kinetic energy was used. From this same definition of kinetic energy:

$$\begin{aligned} K &= \frac{1}{2}\sum_i m_i \boldsymbol{v}_i . \boldsymbol{v}_i \\ dK &= \sum_i m_i \boldsymbol{v}_i . \dot{\boldsymbol{v}}_i dt \end{aligned} \tag{3.38}$$

comparing the last equation above with the last equation in 3.37:

$$\dot{\boldsymbol{v}}_i = \frac{\boldsymbol{v}_i}{2\tau}\left(\frac{T_0}{T} - 1\right) \tag{3.39}$$

which summed with the term $\frac{F_i}{m_i}$ (coming from NVE integration) yields the Berendsen equation 3.16. This thermostat is also compatible with the Nosé-Hoover equations of motion. To see that, it is only required to define the following transformation rules:

$$\begin{aligned} dK &= -2\epsilon K\frac{dt}{\tau} = -\epsilon\sum_i \frac{\boldsymbol{p}_i.\boldsymbol{p}_i}{m_i}\frac{dt}{\tau} \\ d\epsilon &= \left(\frac{K}{\bar{K}} - 1\right)\frac{dt}{\tau} \end{aligned} \tag{3.40}$$

with the definition of dK in terms of momentum, one can obtain:

$$\begin{aligned} dK &= \sum_i \frac{\boldsymbol{p}_i}{m_i}\dot{\boldsymbol{p}}_i dt \quad \textit{by comparing with first equation of 3.40} \rightarrow \\ \dot{\boldsymbol{p}}_i &= -\boldsymbol{p}_i\frac{\epsilon}{\tau} \end{aligned} \tag{3.41}$$

which summing with previous NVE integration, yields:

$$\dot{\boldsymbol{p}}_i = \boldsymbol{F}_i(\{\boldsymbol{q}_i\}) - \boldsymbol{p}_i\frac{\epsilon}{\tau} \tag{3.42}$$

with $\frac{\epsilon}{\tau}$ being the Nosé-Hoover variable ζ (as in second equation of 3.23). From Hoover's equations of motion, the time evolution for ζ can be written as:

$$\begin{aligned} d\zeta &= \frac{1}{Q}\left(\sum_i \frac{\boldsymbol{p}_i.\boldsymbol{p}_i}{m_i} - Nk_BT_0\right)dt \\ d\zeta &= \frac{Nk_BT_0}{Q}\left(\frac{2K}{2\bar{K}} - 1\right)dt \\ d\zeta &= \frac{Nk_BT_0}{Q}\left(\frac{K}{\bar{K}} - 1\right)dt \end{aligned} \tag{3.43}$$

which in terms of ϵ and comparing with the second equation in eq. 3.40 yields the condition for the thermostat mass (Q):

$$\begin{aligned} d\epsilon = \tau d\zeta &= \frac{Nk_BT_0\tau}{Q}\left(\frac{K}{\bar{K}} - 1\right)dt \rightarrow \\ Q &= Nk_BT_0\tau^2 \end{aligned} \tag{3.44}$$

under this condition and the set of equations 3.40, the BDP thermostat yields Nosé-Hoover equations of motion and hence follows the canonical distribution.

3.1.3 Barostats

Another thermodynamical variable that is of interest to control on a simulation is the pressure of the system. Algorithms capable of controling the pressure in MD simulations are called barostats.

3.1.3.1 Berendsen barostat

One of the first popular used Barostats is the one from Berendsen [35]. Its idea is similar to its thermostat (section 3.1.2.1), the system is in weak coupling with an external bath. And the pressure changes of the system with time, are related to the bath's pressure P_0 as:

$$\frac{\mathrm{d}P}{\mathrm{d}t} = \left(\frac{P_0 - P}{\tau_P}\right) \tag{3.45}$$

which implies exponential relaxation of the system's pressure to the target value, through a single relaxation constant τ_P. To achieve this goal, particle coordinates (x_i) together with lattice vectors (l_i) are scaled by a time varying coefficient $\mu(t)$:

$$\begin{aligned} x_i^{'}(t) &= \mu(t) x_i(t) \\ l_i^{'}(t) &= \mu(t) l_i \end{aligned} \tag{3.46}$$

In practice these transformations are achieved by changing the equations of motion of x_i as:

$$\frac{\mathrm{d}x_i^{'}}{\mathrm{d}t} = v_{x_i} + \alpha x_i^{'} \tag{3.47}$$

comparing with the time derivative of first equation in 3.46 we have:

$$\begin{aligned} \frac{\mathrm{d}x_i^{'}}{\mathrm{d}t} &= v_{x_i} + \alpha x_i^{'} \\ \frac{\mathrm{d}x_i^{'}}{\mathrm{d}t} &= \mu \frac{\mathrm{d}x_i}{\mathrm{d}t} + \frac{\mathrm{d}\mu}{\mathrm{d}t} x_i \end{aligned} \tag{3.48}$$

It is easy to see, by comparing the terms on the first equation in 3.48 with the terms on the second equation, that the following exprssions are only valid on the regime that $\mu \approx 1 \rightarrow x_i^{'} \approx x_i$, that is α and dt are small enough (such that weak coupling is valid), then:

$$\begin{aligned} &\mu \approx 1 \\ &\frac{\mathrm{d}\mu}{\mathrm{d}t} = \alpha \rightarrow \mu(t) = 1 + \alpha dt \end{aligned} \tag{3.49}$$

That is, the scaling factor works on the coordinates as if it was instantaneous $x(t + \Delta t) = \mu x(t + \Delta t)$. This fact is implicit on the original Berendsen [35] method. The equation 3.47 implies a volume transformation of the kind:

$$\begin{aligned} &\frac{\mathrm{d}V^{'}}{\mathrm{d}t} = 3\alpha V \\ &\text{with } V^{'} = \mu^3 V \end{aligned} \tag{3.50}$$

Following the same steps as in equation 3.48 for the volume equation leads to an equivalent definition of μ as:

$$\mu(t) = (1 + 3\alpha dt)^{1/3} \tag{3.51}$$

To find alpha, it is necessary to relate the time derivative of pressure with the isothermal compressibility factor k_T as:

$$\begin{gathered} k_T = -\frac{1}{V}\frac{\partial V}{\partial P} \\ \frac{\mathrm{d}P}{\mathrm{d}t} = -\frac{1}{k_T V}\frac{\mathrm{d}V}{\mathrm{d}t} \end{gathered} \tag{3.52}$$

combining the second equation in 3.52 with the transformation rule for volume in 3.50 and 3.45 the value of alpha is obtained:

$$\begin{aligned} \frac{\mathrm{d}P}{\mathrm{d}t} &= -\frac{1}{k_T V}\frac{\mathrm{d}V}{\mathrm{d}t} = -\frac{3\alpha V}{k_T V} \\ -\frac{3\alpha}{k_T} &= \frac{P_0 - P}{\tau_P} \\ \alpha &= -\frac{k_T(P_0 - P)}{3\tau_P} \end{aligned} \tag{3.53}$$

with this the value of μ follows immediately from 3.51 to be:

$$\mu(t) = \left(1 - \frac{k_T(P_0 - P)}{\tau_P} dt\right)^{1/3} \tag{3.54}$$

for an isotropic material. The condition of weak coupling imposes a restriction on the ratio $\frac{\tau_P}{dt}$ which is typically taken to be $\frac{\tau_P}{dt} = 1000$. Despite its simplicity and efficiency to reach the target Pressure value, the Berendsen algorithm does not sample the true NPT ensemble [42], so in situations in which this is required it can not be used.

When required, for an isotropic system, the internal pressure is calculated as :

$$P = \frac{2}{3V}\left(\sum_i m_i \boldsymbol{v}_i . \boldsymbol{v}_i + \sum_{i<j} \mathbf{r}_{ij} . \mathbf{F}_{ij}\right) \tag{3.55}$$

If however, the system is anisotropic a tensor product version of 3.55 can be written as:

$$\mathbf{P} = \frac{1}{V}\left(\sum_i m_i \mathbf{v}_i \otimes \mathbf{v}_i + \sum_{i<j} \mathbf{r}_{ij} \otimes \mathbf{F}_{ij}\right) \tag{3.56}$$

And the equation for the scaling parameter (eq 3.54 in terms of box lenghts) on the anisotropic case changes to:

$$\mu = \mathbf{1} - \frac{k_T dt\,(\mathbf{P}_0 - \mathbf{P})}{3\tau_P} \tag{3.57}$$

Now that we talked about the fundamentals of Molecular Dynamics simulation and how thermostats and barostats work. There can be an explanation about the way heat conductivity is calculated using this technique.

3.2 CALCULATING HEAT CONDUCTIVITY WITHIN MD

Heat conductivity coefficients under the MD framework are usually calculated following two different schemes. The first kind of methods rely on the calculation of fluctuations of the energy current, measured by the integral of its correlation function, under thermal equilibrium conditions (the whole system is in contact with a reservoir at temperature T). These methods rely on the Green-Kubo formula [43, Section 21-8] (eq. 3.58) and are called Equilibrium Molecular Dynamics (EMD) methods.

$$\kappa^{\mu\nu} = \frac{1}{k_B T^2 V} \int_0^\infty \langle J^\mu(t') J^\nu(0) \rangle \, dt' \tag{3.58}$$

where V is the system's volume, k_B is Boltzmann's constant, T is the reservoir temperature, and J^μ is the μ cartesian component of the energy current, that is usually defined as:

$$J^\mu = \frac{\mathrm{d}}{\mathrm{d}t} \left(\sum_{j=1}^{N} r_j^\mu E_j \right) \tag{3.59}$$

where j represents the atom's index and E_j is the total on site energy.

The second approach is based on driving the system out of equilibrium, by imposing a temperature gradient and measuring the response flux [44] (these are called Non Equilbrium Molecular Dynamics (NEMD) methods) or by imposing a heatflux and measuring the temperature gradient as a response [45] (these are called reverse Non Equilibrium Molecular Dynamics (rNEMD) methods).

An intermediate method was also developed, one that posses caracteristics of both equilibrium and out of equilibrium methods. This one was first used by Evans [46] in 1982 (only for twobody potentials) and then recently extended by Fan (2019) [47] for manybody potentials. On this method, a small force is applied to the system such that it is removed from equilibrium, then its not like in the EMD method, were correlation functions of the equilibrium flux generate the heat conductivity response. But, it is also not like the thermostated NEMD methods, due to the fact that no heat flux or temperature gradient is fiercely imposed on the system. The heat conductivity coefficient calculated here, is a result of measuring the heat

current itself on the out of the equilibrium distribution. This out of equilibrium heat current can be related to the equilibrium distribution by a flux correlation function similar to the one in Green-Kubo's formula (eq. 3.58), but with the definition that the flux defined is a response to a small force continuously applied to the system. Given the use of both equilibrium and non equilibrium concepts on the same method, it was named HNEMD. In our work we only used rNEMD and HNEMD to measure the heat conductivity for the Si membranes, so more details will be given for each of these methods at the subsections below.

3.2.1 Reverse Non Equilibrium Molecular Dynamics (rNEMD)

In the case of rNEMD, the whole simulation box is divided in N identical regions, the $l = 1$ region is the cold reservoir, and the $l = N/2+1$ is the hot reservoir. The algorithms follows the procedure developed by Muller-Plathe in 1997 [45]. Basically the algorithm exchange, at each $\mathcal{W}$ steps, the velocity vector from the atom that has the smallest velocity on the hot region (coldest atom) with the one that has the highest velocity in the cold region (hottest atom). By defining the rate of exchange, which we call $\mathcal{W}$, it is possible to control the imposed heat flux on the system. The method is called reverse, because an imposed heat flux generates a temperature gradient on the system, as a response. Which is the contrary of the usual NEMD methods, were a imposed temperature difference generates the heat flux as a response. The heat conductivity is then calculated via Fourier's law as:

$$\kappa_{\mu\mu} = -\frac{\langle J_\mu(t)\rangle}{\langle \nabla T_\mu\rangle} \tag{3.60}$$

where J_μ is the flux in the μ direction, and ∇T_μ is the temperature gradient measured in the same direction as the flux. As mentioned before, the relevant energy that contributes to the flux comes from the difference between kinetic energies from the hottest atom on the cold reservoir (velocity v_h), and the coldest atom on the hot reservoir (velocity v_c). J_μ is then calculated as:

$$J_\mu(t) = \frac{\sum_{exchanges} \frac{m(v_h^2 - v_c^2)}{2}}{2tA} \tag{3.61}$$

$$\tag{3.62}$$

where A is the transversal section area to the μ direction. The factor of two on the denominator accounts for the fact that we use periodic boundary conditions on direction μ.

3.2.2 Homogeneous Non-Equilibrium Molecular Dynamics - HNEMD

In this section we present the ideas behind the HNEMD method based on the same steps as detailed in [46, 47, 48]. The central idea in HNEMD is the application of a small driving force to the system, such that it is removed from equilibrium but still keeps on the regime of linear response theory, under such circumstances the equations of motion are modified such that:

$$\begin{aligned} \dot{\boldsymbol{q}}_i(t) &= \frac{\boldsymbol{p_i}}{m} \\ \dot{\boldsymbol{p}}_i(t) &= \boldsymbol{F_i} + \boldsymbol{D_i}(q_i, p_i)\boldsymbol{F_e} \end{aligned} \tag{3.63}$$

where $\boldsymbol{D_i}$ is, in general a rank two tensor, and F_e is a vector parameter that is time dependent, but here will be taken to be constant in the transport direction of interest. $\boldsymbol{F_e}$ has units of distance^{-1}, such that $\boldsymbol{D_i F_e}$ has units of force.

The term $\boldsymbol{D_i F_e}$ is the driving force responsible to take the system out of equilibrium. Under such conditions the system is no longer Hamiltonian, in the sense that Hamilton's equations do not generate the equations of motion in eq. 3.63. Despite that, the equilibrium Hamiltonian can be thought of as a phase space variable, or phase variable, for short. If the system is not Hamiltonian, the time derivative of the phase variable H is not zero, under the equations of motion 3.63 the derivative is given by [46, 47, 48]:

$$\frac{\mathrm{d}H}{\mathrm{d}t} = -\boldsymbol{J_d F_e} \tag{3.64}$$

where $\boldsymbol{J_d}$ is the dissipative heat (or energy) current vector. On the other hand, the time derivative of the phase variable H can be calculated as:

$$\begin{aligned} \frac{\mathrm{d}H}{\mathrm{d}t} &= \frac{\partial H}{\partial \Gamma}\dot{\Gamma} = \sum_i \frac{\partial H}{\partial \boldsymbol{q_i}}\dot{\boldsymbol{q}}_i + \frac{\partial H}{\partial \boldsymbol{p}_i}\dot{\boldsymbol{p}}_i \\ &= \sum_i -\boldsymbol{F_i}\frac{\boldsymbol{p_i}}{m_i} + \frac{\boldsymbol{p_i}}{m_i}\left(\boldsymbol{F_i} + \boldsymbol{D_i}.\boldsymbol{F_e}\right) \\ \frac{\mathrm{d}H}{\mathrm{d}t} &= -\sum_i \left(-\frac{\boldsymbol{p_i}}{m_i}\boldsymbol{D_i F_e}\right) \end{aligned} \tag{3.65}$$

where Γ denotes all the set of $6N$ phase space variables q_i, p_i with N being the number of particles on the system. By comparing last line in eq. 3.64 with eq. 3.65, the dissipative flux vector can be identified as:

$$\boldsymbol{J_d} = \sum_i -\frac{\boldsymbol{p_i}}{m_i}\boldsymbol{D_i} \tag{3.66}$$

Two more steps are required to derive the relation with the thermal conductivity tensor, identifying J_d and calculating the expectation value of the heat current out of equilibrium. First we try to achieve the latter. The expectation value of a general time evolved phase variable $A(t)$, can be calculated as:

$$\langle A(t)\rangle = \int d\Gamma A(\Gamma,0) f(\Gamma,t) \tag{3.67}$$

$A(\Gamma,0)$ represents the equilibrium value of phase variable A. And $f(\Gamma,t)$ represents time evolution of the equilibrium phase space density $f(\Gamma,0)$. The distribution $f(\Gamma,t)$ follows a Liouville equation, which in the Γ notation can be written as:

$$\frac{\partial f(\Gamma,t)}{\partial t} = -iLf = -\frac{\partial\left(f\dot{\Gamma}\right)}{\partial\Gamma} \tag{3.68}$$

where L is the so called Liouville operator. Under the condition that $\frac{\partial\dot{\Gamma}}{\partial\Gamma} = 0$, the Liouville equation can be simplified to:

$$\frac{\partial f(\Gamma,t)}{\partial t} = -iLf = -\frac{\partial f}{\partial\Gamma}\dot{\Gamma} = -iL_0 f \tag{3.69}$$

where L_0 represents only the part of the Liouvillean that is independent of the external force. Expanding eq. 3.68 and rewritting $f = \Delta f(\Gamma,t) + f(\Gamma,0)$ and $L = \Delta L + L_0$ we end up with:

$$\begin{aligned} \frac{\partial}{\partial t}\left(f(\Gamma,0) + \Delta f(\Gamma,t)\right) &= -i(L_0 + \Delta L)(f(\Gamma,0) + \Delta f(\Gamma,t)) \\ \frac{\partial \Delta f(\Gamma,t)}{\partial t} &= -iL_0\Delta f - i\Delta L f(\Gamma,0) \end{aligned} \tag{3.70}$$

where to get to the second line of eq. 3.70 we used $-iL_0 f(\Gamma,0) = 0$ and take only the first order terms. The formal solution to this linearized Liouville equation, as given by Evans [46, 48] is:

$$\Delta f(\Gamma,t) = -\int_0^t dt' exp[-iL_0(t-t')] i\Delta L(t') f(\Gamma,0) \tag{3.71}$$

which we see that it is indeed the solution because when $t = 0$, $\Delta f = 0$ as it should be. Now we go back to eq. 3.67 and rewrite $f(\Gamma,t) = \Delta f + f(\Gamma,0)$ to obtain:

$$\begin{aligned} \langle A(t)\rangle &= \int d\Gamma A(\Gamma,0)(\Delta f(\Gamma,t) + f(\Gamma,0)) \\ \langle A(t)\rangle &= \int d\Gamma A(\Gamma,0) f(\Gamma,0) + \int d\Gamma A(\Gamma,0)\Delta f(\Gamma,t) \end{aligned} \tag{3.72}$$

the first term on the right rand side of the second line in eq. 3.72 is just the equilibrium average of the phase variable A, substituting the result given in eq. 3.71 for Δf in the previous equation, we obtain:

$$\langle A(t)\rangle = \langle A(0)\rangle - \int d\Gamma A(\Gamma,0) \int dt' exp[-iL_0(t-t')] i\Delta L(t') f(\Gamma,0) \tag{3.73}$$

the action of the operator $i\Delta L$ on $f(\Gamma,0)$ is:

$$i\Delta L f(\Gamma,0) = iLf(\Gamma,0) = \dot{\Gamma}\frac{\partial f(\Gamma,0)}{\partial \Gamma} \tag{3.74}$$

where again the fact that $iL_0 f(\Gamma,0) = 0$ was used. If the system is in contact with a heat reservoir at a temperature T, the equilibrium distribution will follow a Boltzmann type distribution:

$$f(\Gamma,0) = \frac{exp[-\beta H]}{Z(\beta)} \tag{3.75}$$

with $\beta = \frac{1}{k_B T}$ and $Z(\beta)$ the partition function of the system. Substituting eq. 3.75 in eq. 3.74:

$$i\Delta L f(\Gamma,0) = \dot{\Gamma}\frac{\partial f(\Gamma,0)}{\partial \Gamma} = \dot{\Gamma}\frac{\partial f(\Gamma,0)}{\partial H}\frac{\partial H}{\partial \Gamma} \tag{3.76}$$

from first line of equation 3.65, $\frac{\partial H}{\partial \Gamma} = \frac{1}{\dot{\Gamma}}\frac{\mathrm{d}H}{\mathrm{d}t}$, it follows then that:

$$i\Delta L f(\Gamma,0) = \dot{\Gamma}\frac{\partial f(\Gamma,0)}{\partial H}\frac{\partial H}{\partial \Gamma} = \frac{\partial f(\Gamma,0)}{\partial H}\frac{\mathrm{d}H}{\mathrm{d}t} = \beta \boldsymbol{J_d} \boldsymbol{F_e} f(\Gamma,0) \tag{3.77}$$

by using the results that $\frac{\partial f(\Gamma,0)}{\partial H} = -\beta f(\Gamma,0)$ and the result of eq. 3.64 for $\frac{\mathrm{d}H}{\mathrm{d}t}$. Substituting eq. 3.77 back into 3.73 we obtain:

$$\langle A(t)\rangle = \langle A(0)\rangle - \beta \int_0^t dt' \int d\Gamma A(\Gamma,0) exp[-iL_0(t-t')] \boldsymbol{J_d}(\Gamma,0) \boldsymbol{F_e}(t') f(\Gamma,0) \tag{3.78}$$

the exponential of the Liouvillean operator can act backwards on the phase variable A (similar to the Heisenberg interpretation in quantum mechanics where the time evolution operator acts on the operators instead of the states, for example), such that:

$$\langle A(t)\rangle = \langle A(0)\rangle - \beta \int_0^t dt' \left(\int d\Gamma A(\Gamma, t-t') \boldsymbol{J_d}(\Gamma,0) f(\Gamma,0) \right) \boldsymbol{F_e}(t') \tag{3.79}$$

the term under parenthesis is exactly the definition of the time correlation function between A and the components of $\boldsymbol{J_d}$, such that the final expression for the expectation value of a general phase variable $A(t)$ is:

$$\langle A(t)\rangle = \langle A(0)\rangle - \beta \int_0^t dt' \langle A(t-t') \boldsymbol{J_d}(0)\rangle \boldsymbol{F_e}(t') \tag{3.80}$$

this equation is valid in the limit that $\boldsymbol{F_e} \to 0$, which defines the linear response regime. To go from this equation to the connection with the Green-Kubo formula (eq. 3.58), we need to set both phase variables A and $\boldsymbol{J_d}$ equals to J_q^μ and $-\boldsymbol{J_q}$, respectively. With $\boldsymbol{J_q}$ equals to the heat current vector and J_q^μ its μ cartesian component (e.g, x, y or z). Note that we set A to J_q^μ because in our notation we started the derivation with A being a scalar phase variable, but

the derivation could have been carried out with A being a vector. Incorporating the previous modifications, we get:

$$\left\langle J_q^\mu(t) \right\rangle = \left\langle J_q^\mu(0) \right\rangle + \beta \int_0^t dt' \left\langle J_q^\mu(t-t') \boldsymbol{J_q}(0) \right\rangle \boldsymbol{F_e}(t') \tag{3.81}$$

from here to simplify, assuming that $\boldsymbol{F_e}$ is constant (independent of t') and it lies in some given cartesian direction (e.g., $\boldsymbol{F_e} = F_e \hat{\boldsymbol{x}}$). Assuming also that there is no average heat current at equilibrium $\langle \boldsymbol{J_q}(0) \rangle = 0$ and using the Green-Kubo relation we end up with:

$$\begin{aligned} \left\langle J_q^\mu(t) \right\rangle &= \beta \int_0^t dt' \left\langle J_q^\mu(t-t') J_q^x(0) \right\rangle F_e^x \\ \kappa^{\mu x}(t) &= \left\langle J_q^\mu(t) \right\rangle \frac{1}{TVF_e^x} \end{aligned} \tag{3.82}$$

or in general, assuming $\boldsymbol{F_e}$ is constant and only has component in the ν cartesian direction, any of the 9 components on the heat conductivity tensor can be calculated as:

$$\kappa^{\mu\nu}(t) = \left\langle J_q^\mu(t) \right\rangle \frac{1}{TVF_e^\nu} \tag{3.83}$$

Note that if we substitute the expression for $\left\langle J_q^\mu(t) \right\rangle$ in the first equation of 3.82, on the second equation in 3.82, we get back to the Green-Kubo formula (eq. 3.58). That is equivalent to say that this method gives results that are equivalent to the EMD Green-Kubo method.

Differently from the EMD case, the calculation of the correlation function during the simulation run is not required. It is only required to know how to define the heat flux $J_q(t)$ for all times t. Fan [47] write's down the general form of the heatflux $\boldsymbol{J_q}$ for a manybody potential as:

$$\boldsymbol{J_q} = \sum_i \frac{\boldsymbol{p_i}}{m_i} E_i + \sum_{i,j \neq i} \frac{\boldsymbol{p_i}}{m_i} \left(\frac{\partial U_j}{\partial \boldsymbol{r_{ji}}} \otimes \boldsymbol{r_{ij}} \right) \tag{3.84}$$

comparing with the result obtained in eq.3.66 and remembering to set $\boldsymbol{J_d} = -\boldsymbol{J_q}$ we get:

$$\boldsymbol{D_i} = E_i \mathbf{1} + \sum_{j \neq i} \left(\frac{\partial U_j}{\partial \boldsymbol{r_{ji}}} \otimes \boldsymbol{r_{ij}} \right) \tag{3.85}$$

where $\mathbf{1}$ is the identity matrix and $\otimes$ is the outer product or tensor product operation. Therefore $\boldsymbol{D_i}$ is indeed a tensor. So to calculate the heat conductivity coefficient with this method it is only necessary to first apply the force $\boldsymbol{D_i F_e}$ to the system on top of the interaction potential force, subtract from it the mean force on the system (to ensure conservation of momentum which will not be achieved without this procedure, due to the external force). Calculate the heat flux, for each time t, as defined in eq. 3.84 and finally take its time average (ensemble average due to assumed ergodicity) over the total production run time. And them use eq. 3.83 to calculate κ.

3.2.3 Heat current: Spectral Decomposition

Spectral decomposition of transport properties such as conductivity (κ) and conductance (G) can be calculated indirectly by knowing how to spectrally decompose the heat current (J_q). This result can be achieved by Fourier transforming the force-velocity correlation function [49] or equivalently the virial-velocity correlation function [47]. The approach of Saaskilahti [49] requires the definition of an imaginary surface in the middle of the system where one computes the interaction forces at the particles in first half of the system with the ones in the second half (and vice versa, allowing for symmetrization). Whereas the approach of Fan calculates all the interactions on a defined subsystem volume, with no requirement of defining an imaginary surface. Here we follow the approach of Fan, since this is the one implemented on the Graphics Processing Units Molecular Dynamics (GPUMD) software, which we will be using for the MD simulations (more details about the simulation details are given in section 3.3).

The virial-velocity correlation function is, thus, defined as:

$$\mathbf{K}(t) = \sum_{i,j\neq i} \mathbf{r}_{ij}(0) \left\langle \left(\frac{\partial U_j(0)}{\partial \mathbf{r}_{ij}} \mathbf{v}_i(t) \right) \right\rangle_{ne} \tag{3.86}$$

where the sum over i runs over all the particles inside a group of atoms which are inside a given subsystem volume and j runs over all nearest neighbors of i within the potential cutoff distance. At $t = 0$ this coincides directly with the potential part of the general heat current for many-body potentials as given by [50]. Defining the Fourier transform of $K(t)$ as $\tilde{K}(\omega)$, allows to define the reverse Fourier transform of this function as:

$$\mathbf{K}(t) = \int_{-\infty}^{+\infty} \tilde{\mathbf{K}}(\omega) e^{i\omega t} \frac{d\omega}{2\pi} \tag{3.87}$$

setting $t = 0$ and using the fact that the heat current (J_q) must be a real function, we get:

$$\begin{aligned} \mathbf{K}(0) &= \int_{-\infty}^{+\infty} \tilde{\mathbf{K}}(\omega) \frac{d\omega}{2\pi} \\ \mathbf{J}_q &= \int_{0}^{+\infty} \mathrm{Re}\Big\{ 2\tilde{\mathbf{K}}(\omega) \Big\} \frac{d\omega}{2\pi} \\ \mathbf{J}_q(\omega) &= \mathrm{Re}\Big\{ 2\tilde{\mathbf{K}}(\omega) \Big\} \end{aligned} \tag{3.88}$$

with $J_q(\omega)$ being the spectral decomposed potential part of the heat current. Immediately inspired by the equation 3.83 in section 3.2.2, one can define the spectral decomposed heat conductivity as:

$$\kappa^{\mu\nu}(\omega) = \frac{J_q^{\mu}(\omega)}{TVF_e^{\nu}} \tag{3.89}$$

where V is the volume of the specified subsystem (or control volume as in [51]), T is the system's temperature and F_e is the HNEMD external driving force parameter. In S.I units $\kappa(\omega)$ is given in $Wm^{-1}K^{-1}Hz^{-1}$. On the other hand, during an NEMD or rNEMD simulation, conductance can also be spectral decomposed and calculated as:

$$G^{\mu}(\omega) = \frac{J_q^{\mu}(\omega)}{V\Delta T} \tag{3.90}$$

where V is also the subsystem volume and ΔT is the temperature difference between the thermal reservoirs typical of an NEMD simulation. And in S.I units G is given in units of $Wm^{-2}K^{-1}Hz^{-1}$.

3.3 GENERAL SIMULATION DETAILS

Molecular Dynamics simulations were performed inside LAMMPS [52] and GPUMD [53]. To do the simulations, first we created a Si unit cell (inside lammps), oriented in the 100 direction and rotated 45 degrees such that the transport direction corresponds to the 110 direction. First we created membranes with dimensions $2a_0' \times 2a_0' \times 1a_0$, where $a_0' = a_0\sqrt{2}$ due to the orientation on the 110 direction. Then we reconstructed the dimers at the surface of these membranes, in order to avoid excessive phonon scattering in the z direction due to non bonded Si atoms at the membrane's surface. The reconstruction was done according to Fig. 7. Then the $2 \times 2 \times 1$ unit cell was then replicated to create an $10a_0' \times 10a_0' \times 1a_0$ supercells which was the starting point to all of the MD simulations performed here. The value of lattice parameter used for Silicon was taken from National Insitute of Standards and Technology (NIST) website [54] up to four figures of merit as $a_0 = 5.431\ \mathring{A}$.

All GPUMD simulations were done using periodic boundary conditions only on x and y directions. Also, for GPUMD simulations a relaxation protocol was developed as follows, minimize the unit supercell, short temperature equilibration at 900 K (50 ps), longer box relaxation (at 0 bar and 300 K using berendsen barostat in anisotropic conditions) for the duration of 500 ps and finally temperature equilibration at 300 K. The steps involving only temperature equilibration were performed using the BDP thermostat 3.1.2.4 with a coupling constant of $\tau = 0.1$ ps. Standard 1 fs time step was used in all GPUMD simulations. Below there is an example with the input file required to run the simulation within GPUMD. The last block of information on this file is dedicated to the HNEMD run, which will be detailed in the next section.

Figure 7 – Surface dimerization (a) $2a_0' \times 2a_0' \times 1a_0$ Si membrane no dimerization. (b) same membrane as in (a) but with dimerization at the surface. Si atoms were connected upon (red in (a)) the z axis and below (blue in (a)) it in an alternated manner.

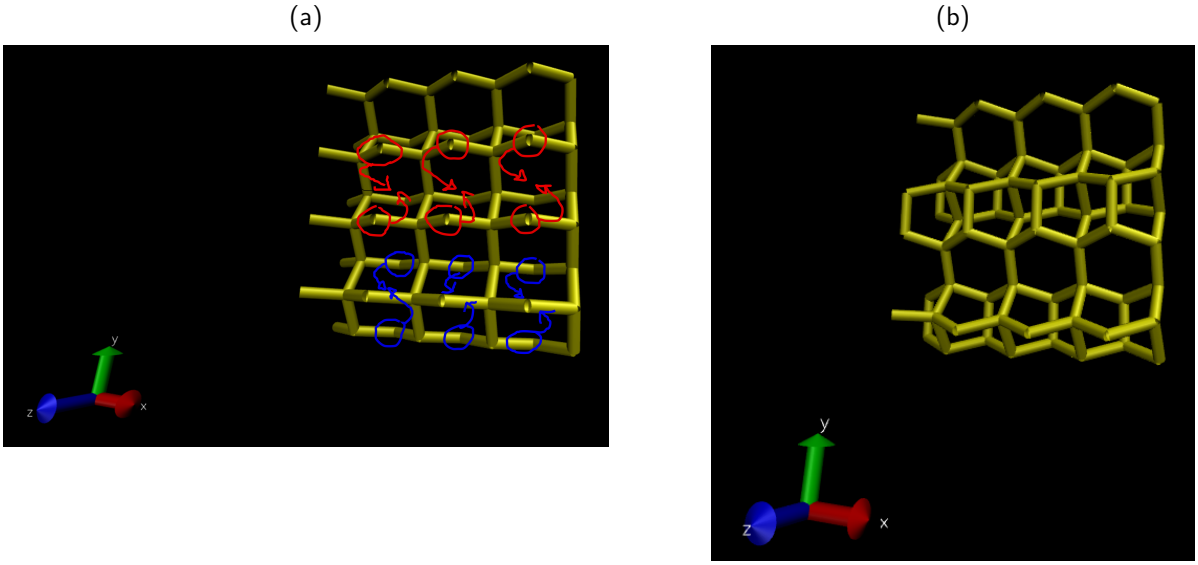

Source: The author (2023)

The rNEMD simulations were performed inside LAMMPS using full periodic boundary conditions and vacumm in the z direction. The structures were minimized, NVT equilibration (NHC thermostat $\tau = 0.1$ ps and 10 chains) for 100 ps at 900 K, then 50 ps at 300 K, then 1 ns relaxation under NPT conditions at 300 K, and finally 50 ps NVT. At this first equilibration and relaxation phase a 1 fs timestep was used. After that, we started the rNEMD simulations. The timestep was changed to 0.1 fs, the energy between hot and cold reservoir was exchanged at each 10000 time steps ($\mathcal{W} = 10000$) and the production run was performed under NVT conditions (NHC thermostat $\tau = 0.1ps$ and 10 chains) until reaching a convergent heat conductivity.

```
potential       Si_Tersoff_1989.txt #ilustration only, full path required here
velocity        300

minimize        sd -1 3000

ensemble        nvt_bdp 900 900 100
dump_exyz       10000 0 0
dump_thermo     1000
run             50000

ensemble npt_ber 300 300 100 0 0 0 100 100 100 1000
dump_exyz       1000 0 0
dump_thermo     1000
dump_restart    500000
```

```
run             500000



ensemble        nvt_bdp 300 300 100
dump_exyz       1000 0 0
dump_thermo     1000
run             50000

ensemble        nvt_bdp 300 300 100
dump_exyz       100000 0 0
dump_thermo     1000
compute_hnemd   1000 1e-5 0 0
compute_shc     5 500 0 1000 120.0
run             15000000
```

Source: The author (2023)

4 RESULTS AND DISCUSSION

As stated at the end of section 1.2, the idea behind this work was to see how the insertion of periodically arranged defects with different geometrical shapes (e.g circles, squares and triangles) would affect the thermal conductivity in 110 direction of these Si membranes. But before getting into the defects we first explored the calculation of thermal conductivity, thermal conductance and other related quantities in the absence of any defects.

4.1 SIZE DEPENDENCE

It is well known that in the case of EMD simulations with the Green-Kubo method the heat conductivity measured scales with system size up to some critical value where it reaches convergence [55, 56, 57]. To explore the presence of such finite size effects in our system, we performed HNEMD simulations with the constant force parameter F_e in eq. (3.83) set to $\mathbf{F_e} = 1 \times 10^{-5}\text{Å}^{-1}\hat{\mathbf{x}}$ which is small enough to keep the system within the regime of linear response theory. The membranes were constructed with dimensions $L \times L \times 1$. In Fig.8 (a and b) we see the time average (for the membrane with $L = 7.681$ nm) over 10 runs of $\kappa_{x,in}(t)$ and $\kappa_{x,out}(t)$, respectively. This heat conductivity decomposition on in-plane and out-of-plane contributions, relies on decomposing the flux in eq. 3.83 on those same components and is the same as done by Fan in [58]. All the HNEMD simulations done here have run for 15 ns, further increase in the simulation time did not seem to change the final values much. So, the value of $\kappa(t)$ will be taken to be sufficiently converged at the end of 15 ns. For this particular case in Fig.8(c) we see that $\kappa_{x,in} >> \kappa_{x,out}$ and the in-plane contribution contributes the most to the total conductivity (in black). Also on Fig.8(d) we see that at 15 ns the only non zero component is κ_{xx}, which is consistent with the fact that the (110) direction coincides with the Si principal axis.

In Fig. 9 we see each of the 10 individual runs before averaging. None of the trajectories are the same, but most of them converge at the end of the 15 ns around their average (within statistical uncertainty).

The same procedure detailed before was repeated for other 4 values of L and the results are summarized in table (1). All values of σ calculated here are estimated as the distribution's standard deviation of final values of κ from plots like the ones in (a-c) in Fig. 9. Column

Figure 8 – HNEMD average data for the membrane with dimensions $L \times L \times 1$ with L=7.681 nm (a) is $\kappa_{x,in}(t)$ in-plane contribution. (b) $\kappa_{x,out}(t)$ out-of-plane contribution. (c)$\kappa_{x,in}(t)$ in red,$\kappa_{x,out}(t)$ in blue and $\kappa_{x,total}(t)$ which is the sum of the previous two (in black). (d)$\kappa_{\nu x}$ with ν=x,y or z.

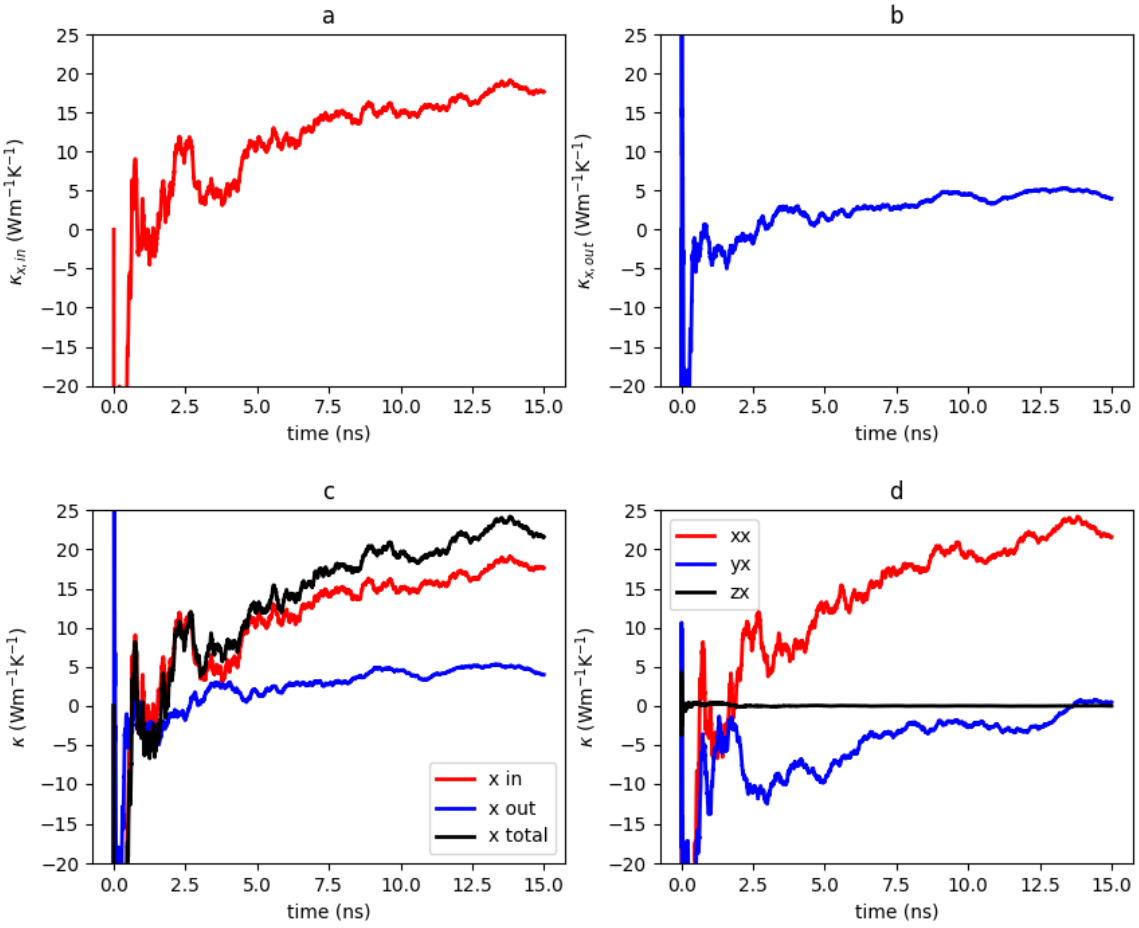

Source: The author (2023)

3 on table 1 shows that total conductivity increases up to $L = 30.72$ nm, where from that point on remains constant. Although the corresponding uncertainty (σ) keeps decreasing with increasing L. The same behaviour can be seen for the in-plane conductivity $\kappa_{x,in}$ and $\kappa_{x,out}$, always with $\kappa_{x,in} >> \kappa_{x,out}$. This is expected as the thickness of the membrane (dimension on z direction) is much smaller than the plane dimensions (x and y) such that the number of modes that contribute to the in-plane conductivity is much larger than the out-of-plane number of phonons.

Using the methods described in section 3.2.3 we proceeded to analyze the size effect on the spectral decomposition of heat conductivity (κ) and heat conductance (G).

Figure 9 – Individual runs data for membrane with dimensions $L \times L \times 1$ with L=7.681 nm (a) is $\kappa_{x,in}(t)$ in-plane contribution. (b) $\kappa_{x,out}(t)$ out-of-plane contribution. (c)$\kappa_{x,total}(t)$

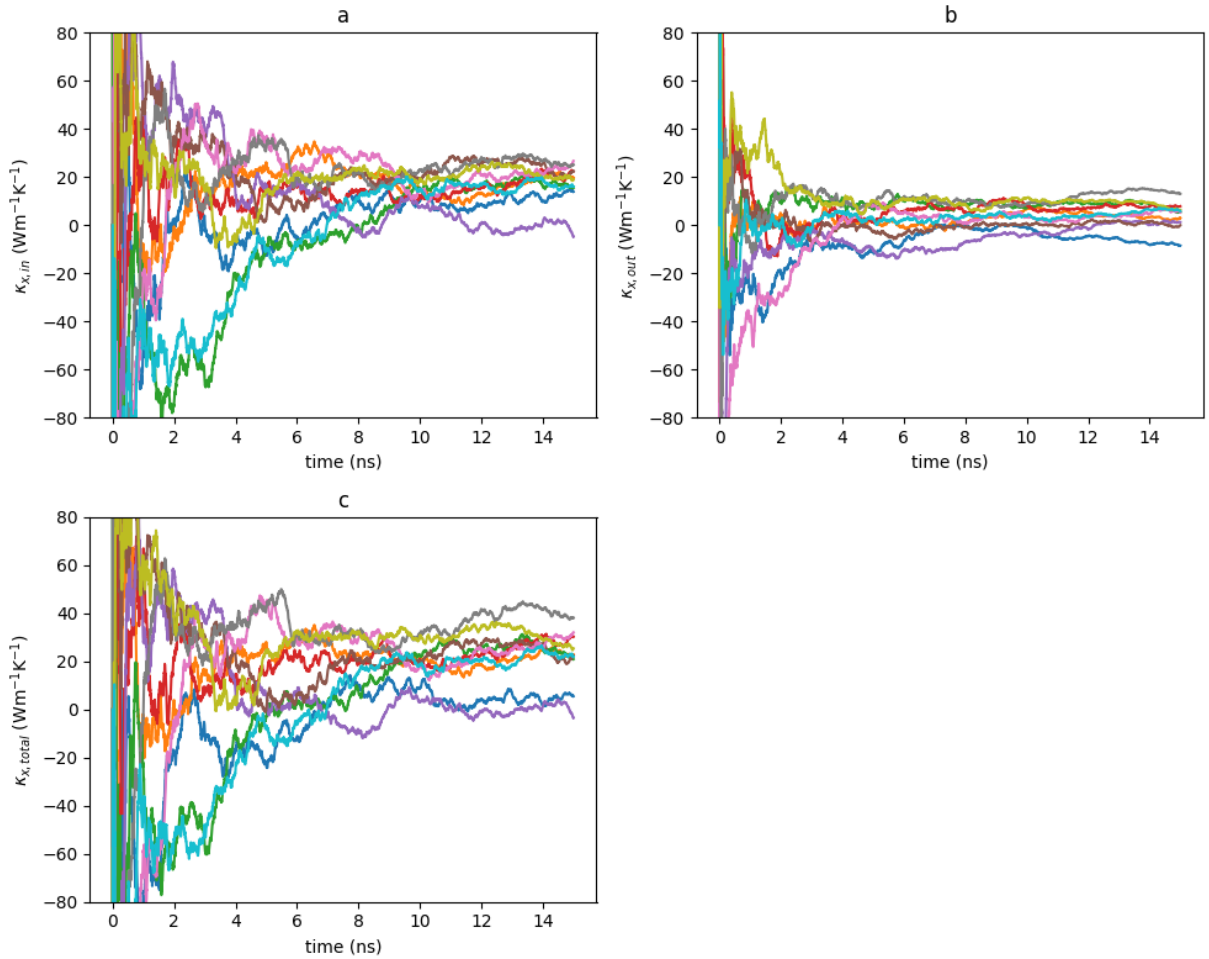

Source: The author (2023)

Table 1 – HNEMD results for Si membranes (10 independent runs)

L (nm)	size $N \times N$ (Na_0')	κ_x (Wm^{-1}K^{-1})	σ	$\kappa_{x,in}$ (Wm^{-1}K^{-1})	σ	$\kappa_{x,out}$ (Wm^{-1}K^{-1})	σ
7.681	10	22	12	17.6	8.4	4.0	5.4
15.36	20	44	11	36.8	8.8	7.6	3.2
30.72	40	60.5	7.5	49.0	6.1	11.5	2.2
53.76	70	65.4	2.8	51.7	2.5	13.65	0.73
69.13	90	61.7	2.5	48.4	1.8	13.31	0.84

Source: The author (2023)

4.1.0.1 Spectral heat conductivity

The spectral heat conductivity (κ) is calculated using the expression in eq. 3.89 which relies on the spectral heat flux $J_q(\omega)$. The spectral heat flux can be obtained by Fourier Transforming the virial-velocity correlation function (eq. 3.86). To accurately sample the virial-velocity correlation function we sampled the data each 5 timesteps, using 500 correlation steps

which results in a total correlation time of 2.5 ps (due to 1 fs simulation time step). Reasonable correlation functions like Fig. 10 were obtained for all the membrane sizes analyzed in table 1. The spectral heat flux for each membrane size was averaged over 10 independent runs and spectral conductivity was calculated as in eq. 3.89 (dividing by an average volume, since each NPT relaxation makes the box sizes slightly different from one another). The spectral conductivities were plotted together in Fig. 11. We can see that for the membranes with dimensions larger than 40×40 ($L = 30.72$ nm) the spectral thermal conductivity plots tend to converge. Also, the integrals on the legend inside Fig. 11 are consistent with the values observed in Column 3 at table 1. That is, the integration values converge for the same membrane size ($N > 40$) as it was obtained in table 1 without considering spectral decomposition. The spectral heat conductivity plot can be interpreted as the average contribution of phonons with frequency f to the thermal conductivity. We see that the modes with small frequency ($f \leq 4.5$ THz) dominate the spectrum.

Figure 10 – Virial-velocity correlation function for the $20a_0' \times 20a_0'$ membrane

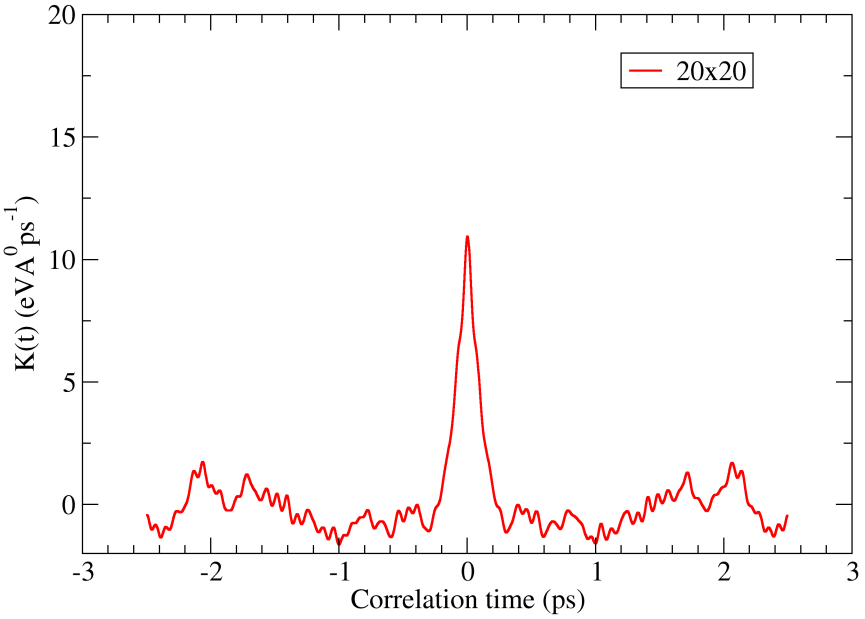

Source: The author (2023)

A point of particular interest is the value at $f = 0$. At this point the optical phonons have zero group velocity ($\frac{\partial \omega}{\partial k} = 0$). In other words, this point corresponds to the contribution to thermal conductivity coming from acoustic modes only. On table (2) we see that as the

Figure 11 – Spectral thermal conductivity as a function of membrane size. On the legend we get the integral of each one of the curves, which corresponds to the total thermal conductivity of the membrane.

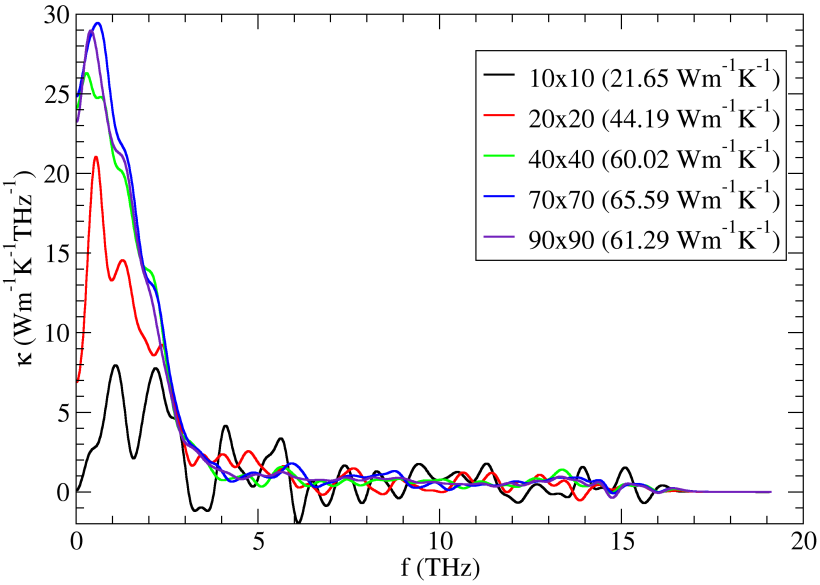

Source: The author (2023)

Table 2 – thermal conductivity at $\omega = 0$, contribution of acoustic phonons, averages over 10 runs

L (nm)	size $N \times N$ (Na_0')	$\kappa_{x,in}$ (Wm^{-1}K^{-1})	σ	$\kappa_{x,out}$ (Wm^{-1}K^{-1})	σ
7.681	10	0.0	2.8	0.1	3.9
15.36	20	3.4	3.1	3.5	4.5
30.72	40	15.0	4.5	9.2	3.9
53.76	70	12.9	2.4	10.0	1.6
69.13	90	12.4	1.3	10.9	1.2

Source: The author (2023)

membrane size increases the $\kappa_{x,in}$ and $\kappa_{x,out}$ at $\omega = 0$ tend towards convergence, again for the membrane sizes with $N > 40$. Also the in-plane and out-of-plane contributions are equivalent in magnitude, that is the longitudinal acoustic phonons (LA), associated with the in-plane, and the transverse acoustic (ZA) phonons, associated with the out-of-plane component, contribute equally to thermal conductivity.

4.1.0.2 Spectral heat conductance

Proceeding the investigation on size effects in membranes with no defects, we evaluated the spectral heat conductance, which is calculated by the expression given in 3.90 (also using a spectral heat flux and volume that are the average over 10 independent runs).

Prior to the calculation of heat conductance the system is divided in groups, where one of them will be fixed, two will be the hot and cold reservoir, and the others will work as intermediate groups. To better explain how the system is divided in such groups, lets take the 20×20 membrane as an example which is represented in Fig.12. For this specific case there is a total of 13 groups, and the group sizes were divided according to the coordinate of the Si atoms in the x direction. The group zero (white in Fig. 12) contain all atoms within $0 \leq x \leq 2a_0'$ and these are kept fixed during all the simulation to avoid kinetic energy drift. Group one (red in Fig. 12) contain atoms between $2a_0' \leq x \leq 6a_0'$ and work as the hot reservoir (coupled to a langevin thermostat with coupling constant $\tau = 0.1$ ps and kept at 310 K) in the NEMD simulation. The last group (blue in Fig. 12), which in this specific case is group 12, works like the cold reservoir (coupled to a langevin thermostat with coupling constant $\tau = 0.1$ ps and kept at 290 K). All the intermediate groups (green in Fig. 12) have $1a_0'$ dimension in the x direction. The spectral heat conductance is calculated only for one of the intermediate groups in Fig. 12 which needs to be as far from the reservoirs as possible. For all the membranes sizes the closest intermediate group to the (left of) membrane's middle was chosen, in this this case of the 20×20 that corresponds to group 6. The volume used in equation 3.90 is the volume of this specific group (subsystem), not the whole system volume.

For all the membrane sizes studied in this section, the hot (red) and cold (blue) reservoirs in Fig. 12 always have $4a_0'$ in the x direction, except for the $10a_0' \times 10a_0'$ where this distance was reduced to $2a_0'$. Changing the size of the reservoir in 10×10 membranes was necessary to have at least one intermediate group (green) to calculate conductance which is not the nearest neighbour group to the reservoir. Apart from the previous exception, all the other membrane sizes have a group zero (size $2a_0'$ in x direction) which is fixed, a group one (size $4a_0'$ in x direction) which is the hot reservoir, a final group (size $4a_0'$ in x direction) and $N - 10$ intermediate groups (each with size $1a_0'$). The spectral heat conductance will then be calculated only into one of the specific intermediate groups, which has index $\frac{N-10}{2} + 1$.

We can see in Fig. 13 that averaging the conductance plot over different runs (3 in this case) and 20 ns production time do not seem to significantly change the curve's shape. Then,

Figure 12 – Membrane NEMD model for thermal conductance calculation ($20a_0' \times 20a_0'$ membrane). Group 0 is fixed, group 1 (in red) is the hot reservoir and group 12 is the cold reservoir (in blue).

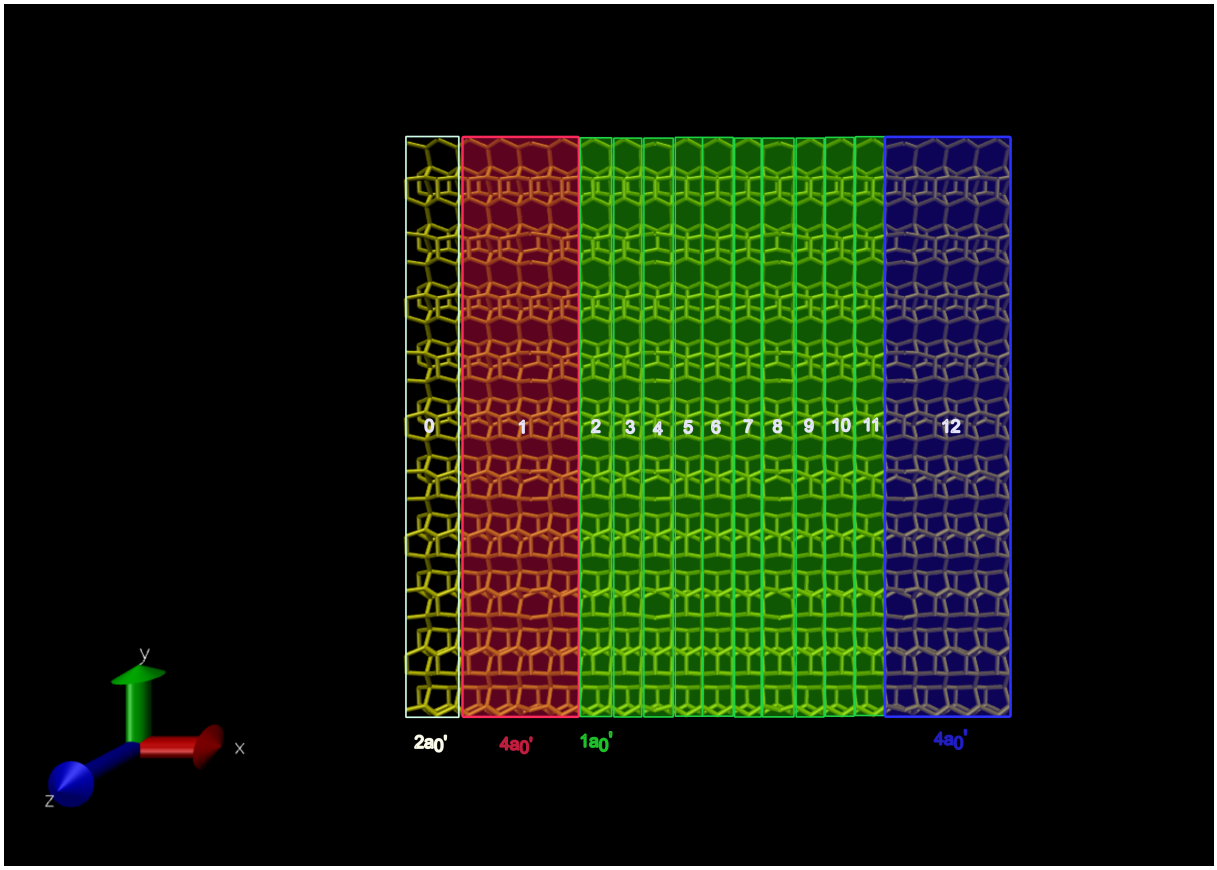

Source: The author (2023)

in order to make sure convergence has been reached, we increased production time to 40 ns and evaluated a single run, instead of averaging the results as we did for $\kappa(\omega)$.

In Fig. 14 we see that as the membrane size increases, the integral over the conductance spectrum starts to converge. Although it keeps decreasing for all membrane sizes used here, the amount of decrease for the membranes with $N \geq 40$ is much smaller than the ones with $N < 40$. The explanation for decreasing conduction could be attributed to the increase in the green region in Fig. 12. As the membrane size increases, the distance between reservoirs also increase, the lifetime of phonons traveling from hot to cold reservoir decreases due to scattering on the way, such that conductance decreases until it eventually reaches its diffusive limit.

Figure 13 – Comparing average spectral conductance with single run spectral conductance for the $10a'_0 \times 10a'_0$ membrane with 20 ns production time.

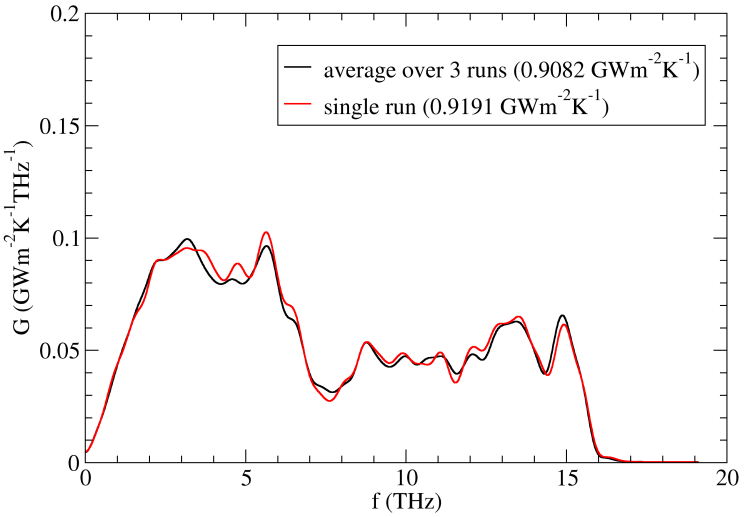

Source: The author (2023)

Figure 14 – Spectral thermal conductance as a function of membrane size. On the legend we get the integral of each one of the curves, which corresponds to the total membranes' thermal conductance.

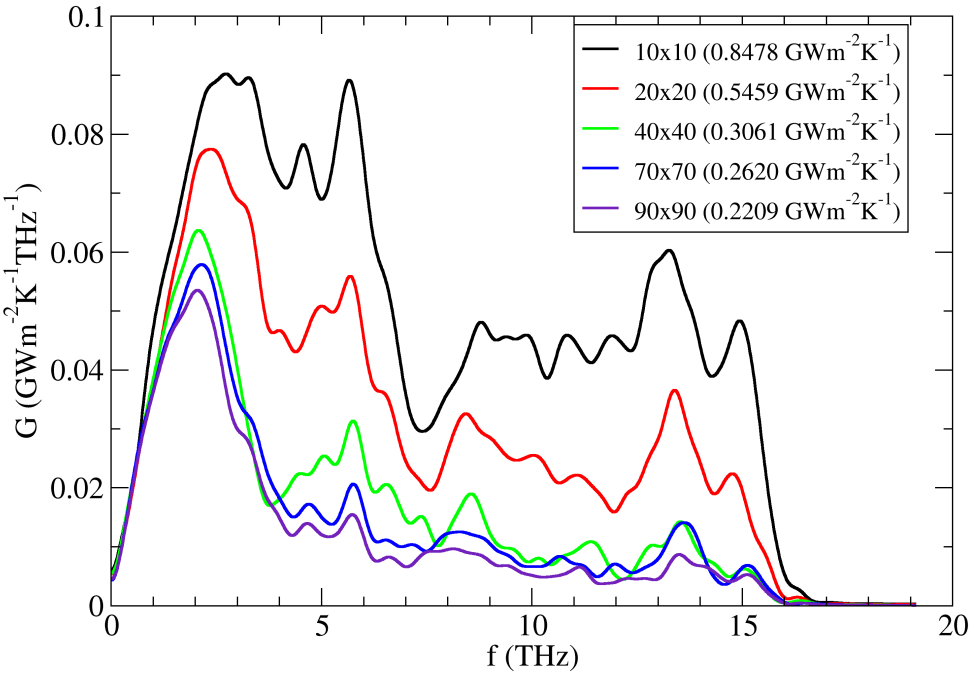

Source: The author (2023)

4.2 DEFECTS

Next we analyzed how the presence of nanometric size holes on the membrane, with different geometric shapes, affects the value of heat conductivity (κ), heat conductance (G) and mean free path (λ). Three different geometrical shapes of defects were investigated: circles, squares and equilateral triangles, as illustrated in Fig. 15. Each defect occupies the center of a supercell with dimensions $10a_0' \times 10a_0'$ which is replicated 7 times in x and y directions, resulting in $70a_0' \times 70a_0'$ membranes. In this first analysis all of the defects are adjusted such that they have the same area of a circle with diameter $5a_0'$, which corresponds to half of the unit supercell size.

Figure 15 – $70a_0' \times 70a_0'$ membranes with defects (a) circles, (b) squares and (c) triangles.

(a) circles

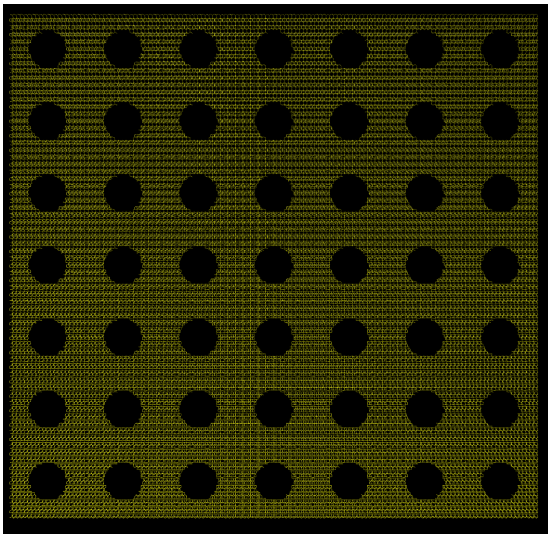

(b) squares

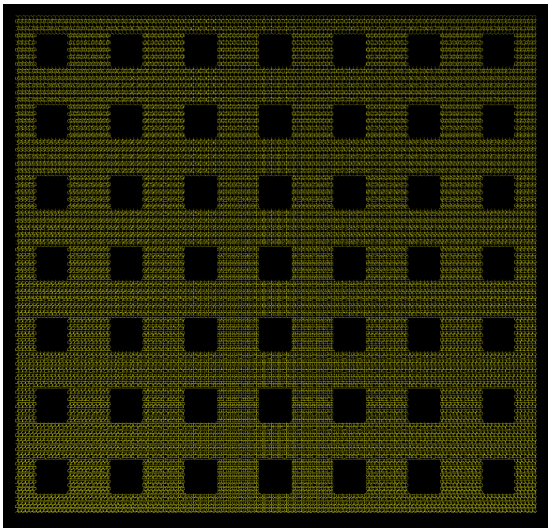

(c) triangles

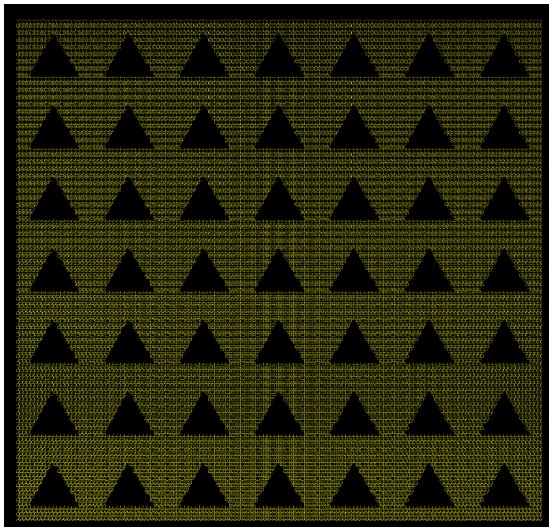

Source: The author (2023)

Table 3 – HNEMD results for Si membranes with defects (average over 10 independent runs)

defect	κ_x ($Wm^{-1}K^{-1}$)	σ	$\kappa_{x,in}$ ($Wm^{-1}K^{-1}$)	σ	$\kappa_{x,out}$ ($Wm^{-1}K^{-1}$)	σ
none	65.4	2.8	51.7	2.5	13.65	0.73
circles	6.12	0.75	5.34	0.93	0.78	0.54
squares	6.04	0.64	5.48	0.59	0.56	0.24
triangles	3.29	0.53	3.01	0.31	0.28	0.35

Source: The author (2023)

As shown in the previous section, the analyses indicated that membranes with $N > 40a_0'$ are effective in producing a converging spectrum, at least in the absence of defects. Given the well-known impact of defects on reducing conductivity due to phonon scattering, we can infer that membranes with $N > 40a_0'$ will continue to suffice even when defects are present. Consequently, we proceeded by fixing the membrane size to $N = 70a_0'$ for all of the further defects studies in this section.

On table (3) we present the final results from HNEMD simulation, where the values of κ are measured after 15 ns of simulation and averaged over 10 runs. The values of κ for membranes with circular and square defects are around 10% of the value where there is no defect. Also the in-plane conductivities dominate the out-of-plane ones. And all the out-of-plane contribution for the cases with defects are near zero, which indicates strong reduction on TA phonon modes contribution to total thermal conductivity in the presence of such scattering centers. There is an almost 50% reduction on total thermal conductivity when comparing triangular defects with the other two. Most of the reduction is due to a decrease on the in-plane thermal conductivity. This difference may be related to nonuniform scattering at the interface between the Si and the vacuum region. If we imagine in-plane phonons coming from $x = 0$ in the unit supercell, they would scatter more or less uniform in the case of a circular interface. The values of conductivity in table 3 also seem to suggest that the same is true for a squared interface. But for the triangular geometry showed in Fig. 16, phonons would reach the interface at different positions due to the triangular symmetry. In terms of waves, phonons would reach the interface with different phases and their recombination after scattering could produce destructive interference decreasing the number of available modes and then by the theory in Chapter 2, with less modes contributing to the sum in eq. 2.18 we have a decrease in total thermal conductivity.

The same patterns observed in table 3 can be seem in Fig. 17, where the spectral contribution of the membrane with no holes (black) is much larger than the cases with defects.

Figure 16 – Phonons (Schematic colored arrows) inside the unit supercell reach the scattering interface at different positions, due to triangular symmetry.

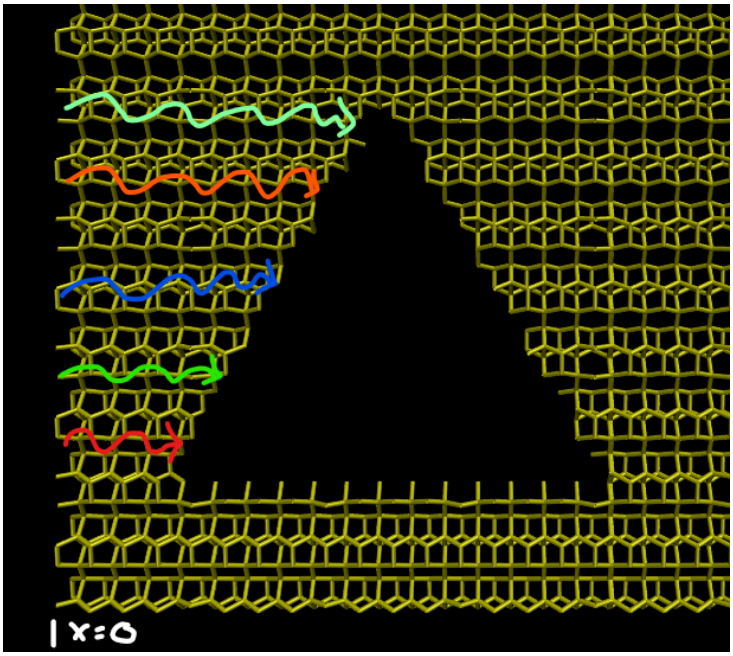

Source: The author (2023)

The largest differences lie in the range of small frequencies ($f \leq 4.3$ THz) which supports the hypothesis that ZA modes are strongly reduced in the presence of defects. Comparing circles (red) and squares (green) there is practically no difference over the entire frequency spectrum. For the triangles, however, there is a systematic decrease in conductance when compared to circles and squares, which covers almost the entire frequency range. The integrals over the entire frequency range are on legend inside Fig.17 and the results are comparable to the ones in table (3).

From spectral conductance data the same trend can be observed. The membrane where there is no defects has the larger conductance, followed by squares and circles which are close to each other and then triangles have the lowest conductance values, see Fig. 18. The largest differences in conductance for the membrane with no defects compared to the others are below 7 THz. This is more evident particularly at the maximum conductance ($f \approx 2.5$ THz), which contributes to its larger integral when compared to the cases with defects. It is difficult to estimate the error associated with the spectral conductance plot, as in principle, each frequency value would have an error bar associated with it. However, by visualizing the integrated values for spectral conductance (legend inside Fig. 18) it is reasonable to say that triangles have the smallest total conductance G between all the membranes studied here. The low to middle frequency region in the spectrum ($f \leq 7$ THz) seems to be the one that contributes the most

Figure 17 – Spectral thermal conductivity as a function of defects. On the legend we get the integral of each one of the curves, which corresponds to the total thermal conductivity of the specified membrane.

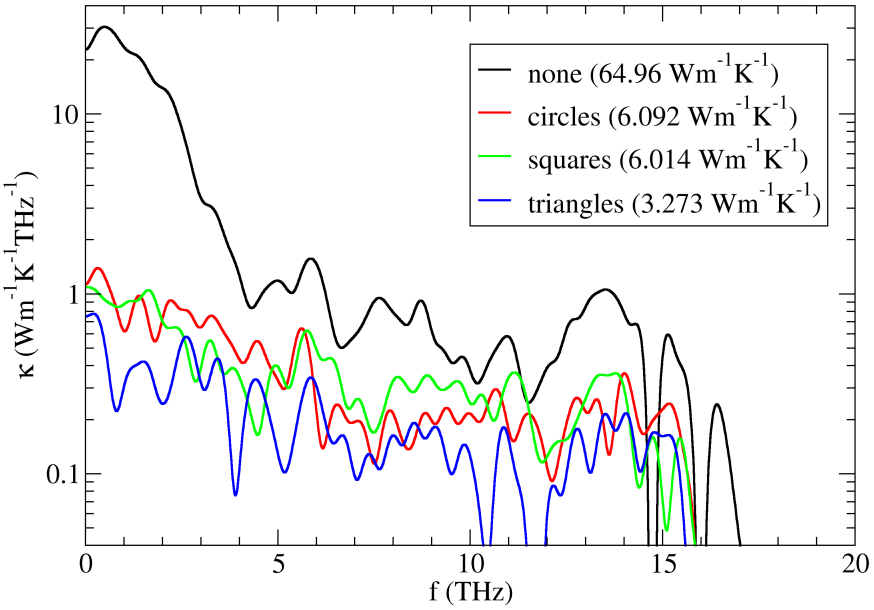

Source: The author (2023)

for this decrease.

4.2.0.1 Mean free path

There is a mathematical relation between heat conductance (G) and heat conductivity (κ) [47, 59]. As κ depends on the sample length, G does not :

$$G = \frac{\kappa}{L} \tag{4.1}$$

this implies that the ratio between κ and G, gives an estimate of the characteristic length in the sample, which can be used as an estimate for the phonon mean free path under certain conditions (see appendix B in [47]). As κ and G depend on the frequency, it is natural to extend the relation 4.1 to the frequency dependent mean free path, as:

$$\lambda(\omega) = \frac{\kappa(\omega)}{G(\omega)} \tag{4.2}$$

under the condition that κ is calculated in the diffusive limit and G corresponds to the ballistic conductance. In Fig. 19a we observe the mean free path as a function of frequency for the

Figure 18 – Spectral thermal conductance as a function of defect shape. On the legend we get the integral of each one of the curves, which corresponds to the total membranes' thermal conductance.

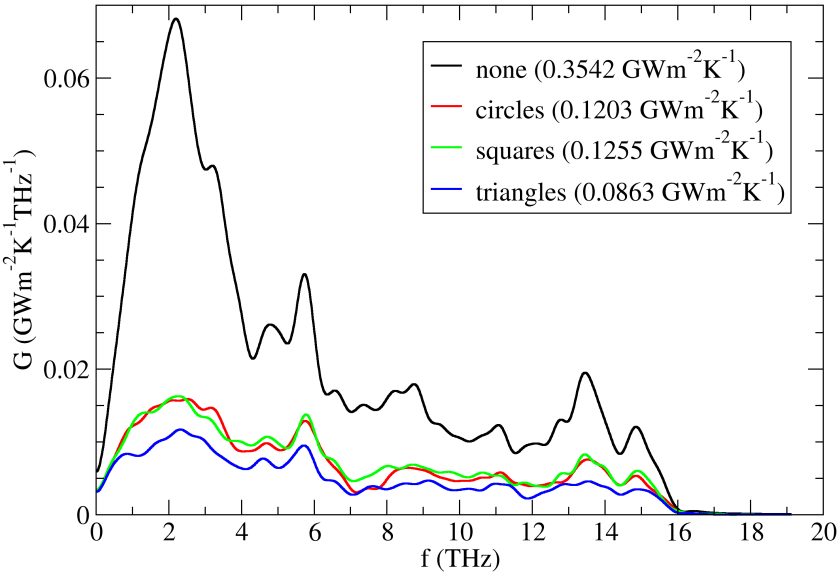

Source: The author (2023)

different membranes. It is clear that the presence of defects results in a reduction in the mean free path in the low frequency limit ($f \leq 3.5$ THz). However, in the high frequency limit ($f = 16.5$ THz) there is also a reduction in λ. The appearance of such a high frequency peak on the spectrum may be associated to a slow decaying phonon due to the "artificial dimerization" done at the membrane's surface when creating the structures. Due to this, we believe that the results for this high frequency regime observed in the spectrum, may not be so reliable, due to the fact that some values of λ show nonphysical negative values at this high frequency limit. The responsible for this negative λ values should be the poor statistical averaging, indicating the requirement of more than 10 runs to improve the predictions of λ in such high frequency limit. Despite that, for the semi quantitative analysis we are doing here, 10 runs should suffice. The comparison in Fig. 19b show that the squares and circles have similar values of λ, but the triangles have a value that is 18% smaller than the value for the circles. Showing that the observed decrease in conductivity and conductance, for the triangles, also results in a decrease in mean free path values.

Figure 19 – Spectral mean free path for the $70a_0' \times 70a_0'$ membranes as a function of defect geometry (a) including the membrane with no defects, (b) data only for circles, squares and triangles.

(a)

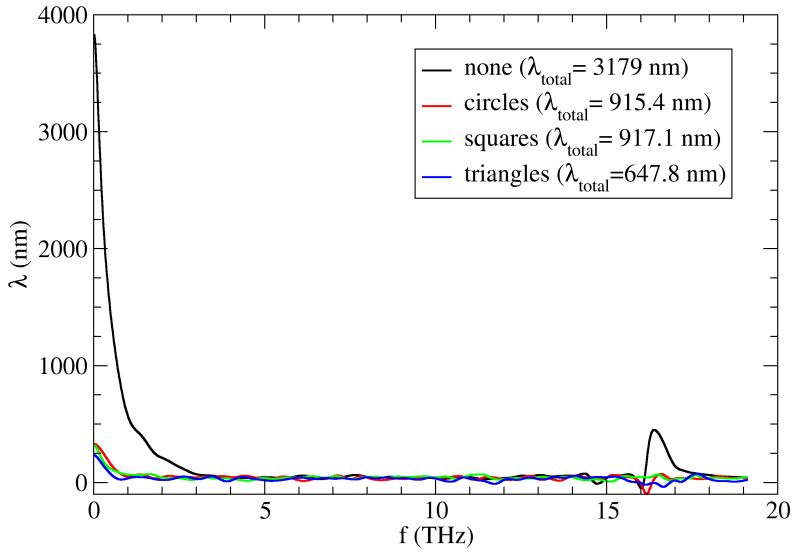

(b)

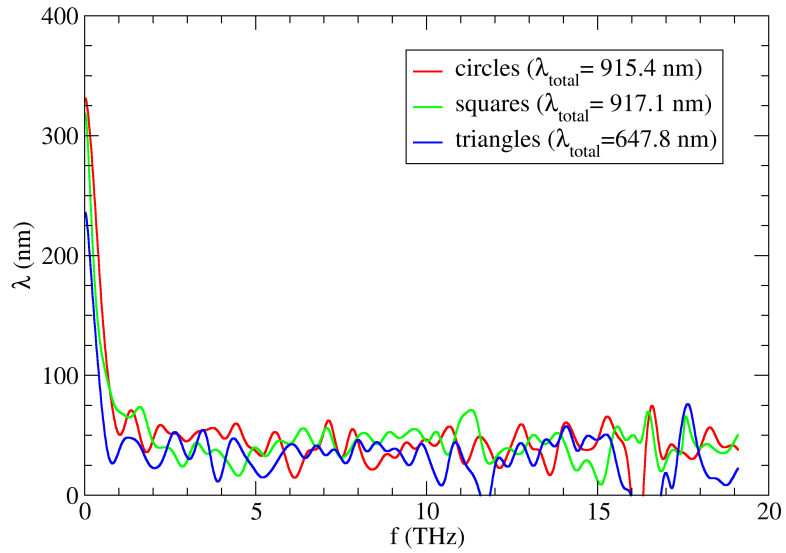

Source: The author (2023)

4.3 LENGTH DEPENDENCE

When performing NEMD simulations to calculate heat conductivity, where the length dependence has to performed in order to get to the true diffusive, its customary to use the ballistic to diffusive formula [47, 58, 60]:

$$\kappa(L) = \frac{\kappa_{diff}}{1 + \frac{\lambda}{L}} \tag{4.3}$$

where λ is an effective mean free path and κ_{diff} is the thermal conductivity in the diffusive limit, when $L \to \infty$. Under the framework of spectral decomposition $\kappa_{diff} = \kappa_{diff}(\omega)$ and $\lambda = \lambda(\omega)$ both depend on frequency. This allows to define the length dependent thermal conductivity as:

$$\kappa(L) = \int_0^\infty \frac{d\omega}{2\pi} \kappa(L, \omega) = \int_0^\infty \frac{d\omega}{2\pi} \frac{\kappa_{diff}(\omega)}{1 + \frac{\lambda(\omega)}{L}} \tag{4.4}$$

where $\kappa(L, \omega)$ is the frequency dependent analogue of eq. 4.3 and takes into account the average contribution of all available phonon modes with frequency ω for a given sample size L, resulting in a better model than eq. 4.3.

In Fig. 20a we can see the length dependent thermal conductivity calculated using eq. 4.4. The membrane with no defects, once again, is the one with largest thermal conductivity, for all L values. As L goes to infinity the length dependent conductivity converge to the spectral conductivity integral, over the entire frequency range (values on the legend inside Fig. 17). In Fig. 20b we see that circles and squares have the same conductivity over the entire length scale, but triangles always have a length dependent conductivity that is smaller than the other two, as a result of having smaller mean free path and smaller spectral conductivity.

Figure 20 – Length dependent thermal conductivity calculated by the expression in eq. 4.4, from 10 to 10^8 nm: (a) all membranes, (b) only the ones with defects.

(a)

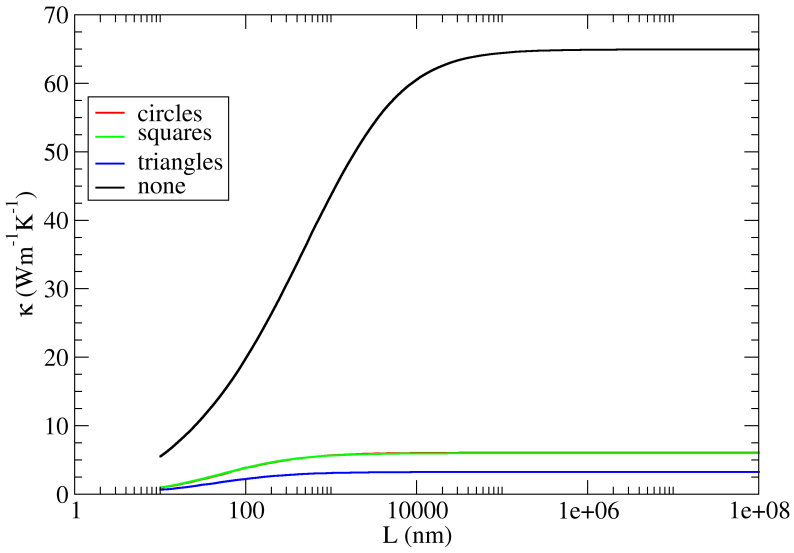

(b)

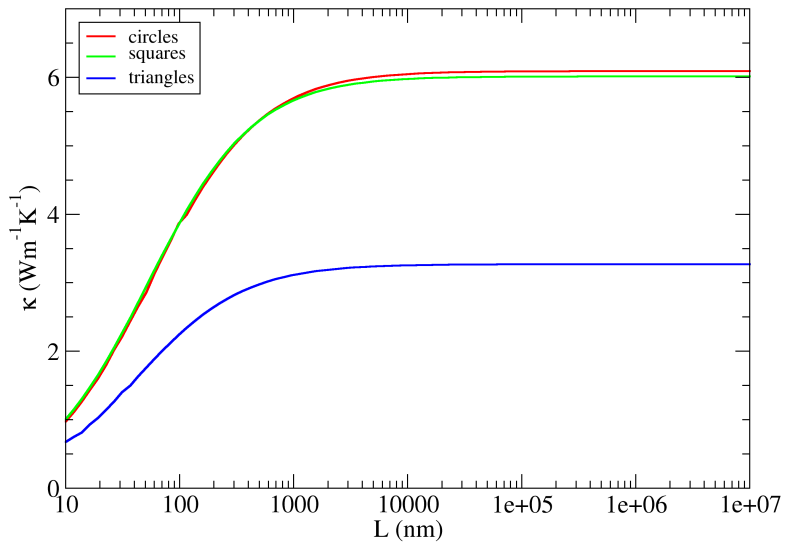

Source: The author (2023)

4.4 COMPARISON TO RNEMD RESULTS

To check if our results are consistent we choose to compare the length dependent thermal conductivity $\kappa(L)$ for the membrane with no defects obtained in the previous section, with a $\kappa(L)$ obtained from rNEMD using the Muller-Plathe method. The plots can be seen in Fig. 21. The conductivity values obtained with the MP method are systematically below the curve obtained with HNEMD. We believe that the disagreement between the two methods is related to the large temperature differences observed within MP. As we can not control the temperature differences in MP, only the rate of kinetic energy exchange, as detailed in sec. 3.2.1 it may happen that the temperature differences may converge to a value that produces a gradient which is too large to keep the linear regime required by Fourier Law. For the largest simulated membrane size the ΔT values converged to 100 K, which is indeed a large temperature difference. To put this in a mathematical form, the heat conductivity in the MP method is calculated assuming Fourier law as:

$$\kappa_{calc,x} = -\frac{J_x}{(\nabla T)_x} \tag{4.5}$$

Thinking in terms of Taylor expanding the heat flux beyond first order, we get:

$$J_x = -\kappa_{true,x}\frac{\mathrm{d}T}{\mathrm{d}x} + \sum_{n\geq 2}\frac{c^n}{n!}\frac{d^nT}{dx^n} \tag{4.6}$$

where the second term in the right hand side represents the higher order terms, beyond linearity. Combining expressions in eq. 4.6 with the one in eq. 4.5 we get:

$$\kappa_{calc,x} = \kappa_{true,x} - \sum_{n\geq 2}\frac{c^n}{n!}\frac{d^{n-1}T}{dx^{n-1}} \tag{4.7}$$

which shows that the calculated value would be below the true thermal conductivity value if the higher order terms are important, which is the case when the gradient is not to small. The diamonds in Fig. 21 considers the gradient to be the difference between the hot and cold thermostat divided by the effective path between the reservoirs, which is taken to be $L = L_x/2$. The crosses are defined by taking the gradient to be the (absolute) average of the linear fit angular coefficients at the two linear parts on a temperature profile, such as the one in Fig. 22. Note that in a profile like this, the temperature difference between the hot and cold reservoirs has always a larger gradient than the linear fit region. As a result, the crosses are closer than diamonds to the HNEMD curve , due to the fact that their gradients in eq. 4.7 are smaller. If that is the reason why we did not find an agreement between the two methods,

using a method that allows for the control of the temperature gradient (such as NEMD using a langevin thermostat) would be preferable instead of an rNEMD method like MP. As even smaller gradients would be required to reach the HNEMD curve.

We are aware that according to Zheng Li *et. al* [59] the correct way to compute the temperature gradient is the one represented in Fig. 21 by diamonds, where the whole temperature difference between thermostats is taken into account, not just the gradient of the linear region. But analyzing the difference between the Zheng Li method (diamonds) and the linear fit region (crosses) offered us intuition to see that the incompatibility in HNEMD and rNEMD data may be related to the large temperature gradients observed inside rNEMD, which is something that we need to explore in future work.

Figure 21 – Comparing the results obtained by HNEMD with the ones obtained in Muller-Plathe method

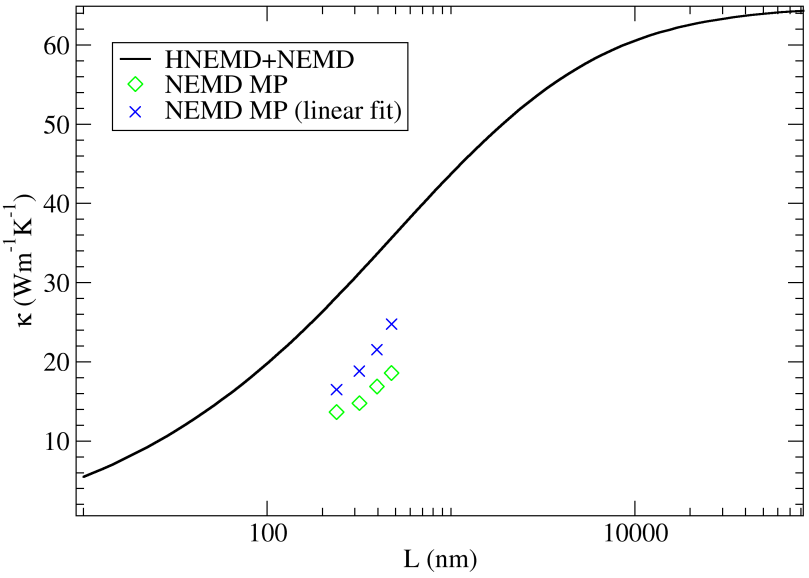

Source: The author (2023)

Figure 22 – Average temperature profile for Si membrane with no defects and $L = 477.11$ nm

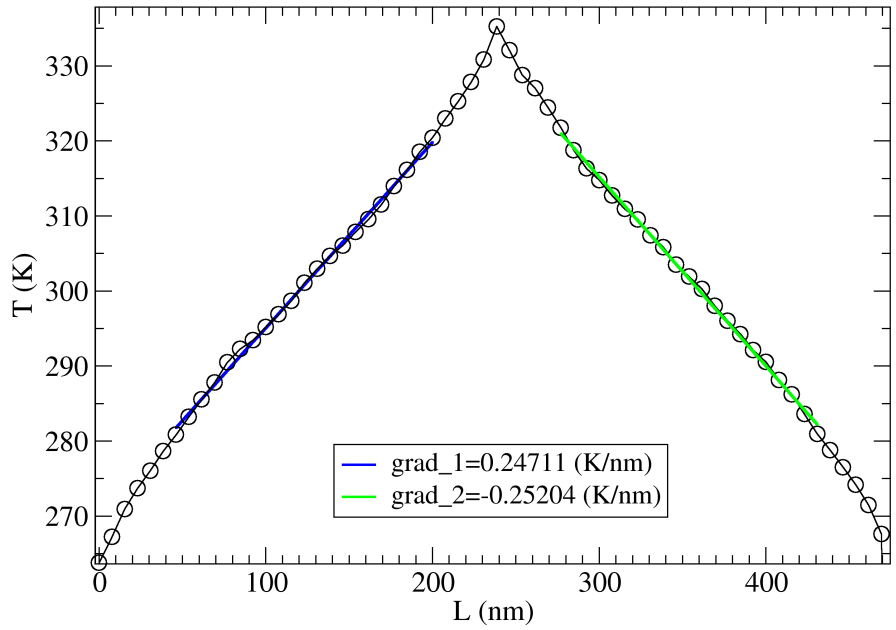

Source: The author (2023)

4.5 DEFECT SIZE DEPENDENCE

It is well known from literature that changing the density of the material by creating holes in the structure, as in the case of phononic crystals, has an effect on the material properties such as elastic constants and heat conductivity [14, 61]. Increasing the defect's area (decreasing its density) results in a decrease in thermal conductivity.

As another test to verify the consistence of our results, we use circular defect membranes to see if changing the circle's diameter has some effect in the measured heat conductivity. On table 4, we see that as the defect's diameter increase the heat conductivity decreases

Table 4 – Si membranes Heat conductivity with circular defects as a function of defect's diameter (averaged over 10 HNEMD runs)

diameter (a_0')	κ_x (Wm^{-1}K^{-1})	σ	$\kappa_{x,in}$ (Wm^{-1}K^{-1})	σ	$\kappa_{x,out}$ (Wm^{-1}K^{-1})	σ
3	11.36	0.81	9.61	0.83	1.75	0.25
5	6.12	0.75	5.34	0.93	0.78	0.54
7	2.82	0.61	2.58	0.55	0.23	0.29

Source: The author (2023)

monotonically. Both the in-plane and out-of-plane components show a decrease, with the out-of-plane component going to zero for the largest diameter (third row on table 4). That shows the possibility of completely removing the contribution of ZA modes to thermal conductivity by increasing the defect size on these Si membranes.

In Fig. 23 we see the length dependent conductivity and the spectral data for these membranes. Both spectral conductivity ($\kappa(f)$) and conductance ($G(f)$) in Fig. 23a and 23b show a decrease over the entire frequency spectrum as the defect size is increased. That is, removing Si atoms from the membranes makes the conductivity and conductance decrease, as expected, due to density differences. These observations also corroborates with data in table 4.

Figure 23 – Spectral data and length dependent conductivity for $70a_0' \times 70a_0'$ Si membranes with circular defects as a function of defect's diameter (a) conductivity, (b) conductance, (c) mean free path and (d) length dependent conductivity.

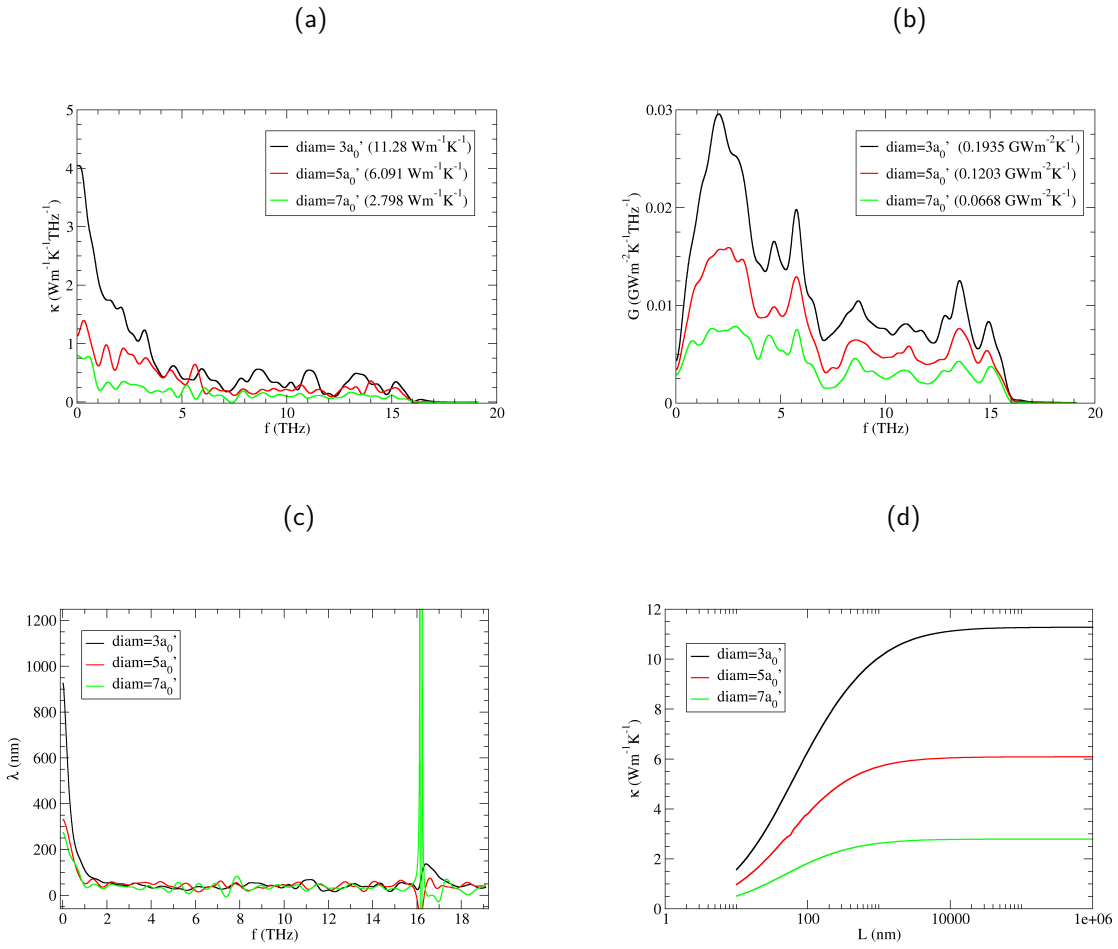

Source: The author (2023)

In Fig. 23c it is possible to see a mean free path decrease for small frequencies ($f \leq 1.5$ THz). For frequencies higher than 1.5 THz the spectral mean free paths are very similar

between the three kinds of membranes over almost the entire frequency range, except in the high frequency limit. As also verified in section 4.2.0.1, the large frequency limit seem to show unreliable results. For frequencies near 16 THz there is a divergence in $\lambda(f)$ for the membrane with the largest defect diameter ($7a_0'$) and some negative mean free path values are also observed. Those again could be related with the dimerization at the surface.

The dimerization was introduced to minimize the problem that the Si atoms at the surface remained without its dimers. Despite that, it can not be done perfectly. Some of the atoms at the membrane surface still remain not bonded to a dimer. These imperfections can artificially create high frequency phonons that do not decay due to phonon scattering and show artificially infinite mean free paths, particularly at those high frequencies. The negative values could also be associated with insufficient statistics.

The length dependence, Fig. 23d, shows that for the larger defects ($5a_0'$ and $7a_0'$) it takes about 900 nm samples to get close to the diffusive limit ($\kappa(L \to \infty)$) where in the case of the smallest defect ($3a_0'$) a sample with more than 10000 nm is required. Which means increasing the removed area makes the length dependent thermal conductivity convergence be reached with a smaller material sample size.

5 CONCLUSIONS

In this work, we verified that introducing periodic defects with different geometrical shapes in Si membranes decreases their thermal conductivity in the 110 direction, even though the area of each defect is set to be the same. This decrease is the same whether the defect has a square or circular geometry (around 90% reduction compared to the membrane with no defects). However, the triangular ones seem to produce a larger decrease in thermal conductivity (around 95 $\%$). When comparing circles ($\kappa = 6.116$ Wm^{-1}K^{-1}) and squares ($\kappa = 6.037$ Wm^{-1}K^{-1}), with triangles ($\kappa = 3.290$ Wm^{-1}K^{-1}), we get that in triangles we have a 46% reduction in thermal conductivity. Spectral decomposition of thermal conductivity κ, thermal conductance G and mean free path λ validates this observation. Triangular defects seem to be special and have a lower thermal conductivity than the other two shapes. Reduction of the spectral quantities at the low frequency regime, seems to be the responsible for the observed decreases in total thermal conductivity. The *in/out plane* decomposition also shows that the contribution of ZA phonon modes to thermal conductivity goes to zero, as any kind of defects is introduced in the membrane.

In terms of physically interpreting the results, it is reasonable to expect that at the interface between Si and the vacuum region, in the case of circular defects, the phonon scattering happens homogeneously. That is, thinking in the phonon as a particle moving inside the unit cell, it could hit the interface at any position, and the resulting scattering would be equivalent to the one observed at any other position at the interface, due to circular symmetry. The square geometry seem to produce that same effect (due to similar values of κ to the circles), at least when looking to the thermal conductivity in the x direction, as we are doing here. However, the triangular symmetry introduces the possibility of the phonon reaching the interface at nonequivalent positions, as showed in Fig. 16, which contributes to inhomogeneous scattering decreasing the mean free paths at lower frequencies. Or if one wants to think in terms of a wave interpretation, a destructive interference arises due to the different phases involved, which contributes to a decrease in the number of available modes and hence decreases the overall thermal conductivity in the x direction.

As future work, we intend to evaluate how the orientation of the defect affects the thermal conductivity. If there is a dependence with the shape of the interface Si-vacuum, spinning the triangle along the C_3 axis of symmetry should change the observed thermal conductivity. Also

could be of interest to increase the membrane thickness and temperature in order to quantify the thermal conductivity dependence on those quantities.

REFERENCES

1 GLASSBRENNER, C. J.; SLACK, G. A. Thermal conductivity of silicon and germanium from 3 k to the melting point. *Physical review*, APS, v. 134, n. 4A, p. A1058, 1964.

2 OLIVA, A.; LUGO, J.; GURUBEL-GONZALEZ, R.; CENTENO, R.; CORONA, J.; AVILéS, F. Temperature coefficient of resistance and thermal expansion coefficient of 10-nm thick gold films. *Thin Solid Films*, v. 623, p. 84–89, 2017. ISSN 0040-6090. Disponível em: <https://www.sciencedirect.com/science/article/pii/S0040609016308410>.

3 UEMOTO, M.; KUWABARA, Y.; SATO, S. A.; YABANA, K. Nonlinear polarization evolution using time-dependent density functional theory. *The Journal of Chemical Physics*, v. 150, n. 9, p. 094101, 03 2019. ISSN 0021-9606. Disponível em: <https://doi.org/10.1063/1.5068711>.

4 SHOCKLEY, W.; QUEISSER, H. J. Detailed balance limit of efficiency of p-n junction solar cells. *Journal of applied physics*, American Institute of Physics, v. 32, n. 3, p. 510–519, 1961.

5 RADZIEMSKA, E.; KLUGMANN, E. Thermally affected parameters of the current–voltage characteristics of silicon photocell. *Energy Conversion and Management*, v. 43, n. 14, p. 1889–1900, 2002. ISSN 0196-8904. Disponível em: <https://www.sciencedirect.com/science/article/pii/S0196890401001327>.

6 CHENG, Z.; LIANG, J.; KAWAMURA, K.; ZHOU, H.; ASAMURA, H.; URATANI, H.; TIWARI, J.; GRAHAM, S.; OHNO, Y.; NAGAI, Y. et al. High thermal conductivity in wafer-scale cubic silicon carbide crystals. *Nature Communications*, Nature Publishing Group UK London, v. 13, n. 1, p. 7201, 2022.

7 MORKOC, b. H.; STRITE, S.; GAO, G.; LIN, M.; SVERDLOV, B.; BURNS, M. Large-band-gap sic, iii-v nitride, and ii-vi znse-based semiconductor device technologies. *Journal of Applied physics*, American Institute of Physics, v. 76, n. 3, p. 1363–1398, 1994.

8 LIANGCHUN, C. Y.; DUNNE, G. T.; MATOCHA, K. S.; CHEUNG, K. P.; SUEHLE, J. S.; SHENG, K. Reliability issues of sic mosfets: A technology for high-temperature environments. *IEEE Transactions on Device and Materials Reliability*, IEEE, v. 10, n. 4, p. 418–426, 2010.

9 VRIES, M. O. de; SATO, S.-i.; OHSHIMA, T.; GIBSON, B. C.; BLUET, J.-M.; CASTELLETTO, S.; JOHNSON, B. C.; REINECK, P. Fluorescent silicon carbide nanoparticles. *Advanced Optical Materials*, v. 9, n. 20, p. 2100311, 2021. Disponível em: <https://onlinelibrary.wiley.com/doi/abs/10.1002/adom.202100311>.

10 ZHENG, Q.; LI, C.; RAI, A.; LEACH, J. H.; BROIDO, D. A.; CAHILL, D. G. Thermal conductivity of gan, gan 71, and sic from 150 k to 850 k. *Physical Review Materials*, APS, v. 3, n. 1, p. 014601, 2019.

11 NEOGI, S.; DONADIO, D. Thermal transport in free-standing silicon membranes: influence of dimensional reduction and surface nanostructures. *The European Physical Journal B*, Springer, v. 88, p. 1–9, 2015.

12 ANUFRIEV, R.; WU, Y.; ORDONEZ-MIRANDA, J.; NOMURA, M. Nanoscale limit of the thermal conductivity in crystalline silicon carbide membranes, nanowires, and phononic crystals. *NPG Asia Materials*, Nature Publishing Group UK London, v. 14, n. 1, p. 35, 2022.

13 BECKER, J. N.; BECHER, C. Coherence properties and quantum control of silicon vacancy color centers in diamond. *physica status solidi (a)*, Wiley Online Library, v. 214, n. 11, p. 1700586, 2017.

14 PENNEC, Y.; VASSEUR, J. O.; DJAFARI-ROUHANI, B.; DOBRZYńSKI, L.; DEYMIER, P. A. Two-dimensional phononic crystals: Examples and applications. *Surface Science Reports*, v. 65, n. 8, p. 229–291, 2010. ISSN 0167-5729. Disponível em: <https://www.sciencedirect.com/science/article/pii/S0167572910000555>.

15 CANG, Y.; JIN, Y.; DJAFARI-ROUHANI, B.; FYTAS, G. Fundamentals, progress and perspectives on high-frequency phononic crystals. *Journal of Physics D: Applied Physics*, IOP Publishing, v. 55, n. 19, p. 193002, 2022.

16 MEHANEY, A.; AHMED, A. M. Locally resonant phononic crystals at low frequencies based on porous sic multilayer. *Scientific reports*, Nature Publishing Group UK London, v. 9, n. 1, p. 14767, 2019.

17 LUCKLUM, F.; VELLEKOOP, M. J. Realization of complex 3-d phononic crystals with wide complete acoustic band gaps. *IEEE transactions on ultrasonics, ferroelectrics, and frequency control*, IEEE, v. 63, n. 5, p. 796–797, 2016.

18 POURABOLGHASEM, R.; MOHAMMADI, S.; EFTEKHAR, A. A.; KHELIF, A.; ADIBI, A. Experimental evidence of high-frequency complete elastic bandgap in pillar-based phononic slabs. *Applied Physics Letters*, AIP Publishing LLC, v. 105, n. 23, p. 231908, 2014.

19 FLOREZ, O.; ARREGUI, G.; ALBRECHTSEN, M.; NG, R.; GOMIS-BRESCO, J.; STOBBE, S.; SOTOMAYOR-TORRES, C.; GARCÍA, P. D. Engineering nanoscale hypersonic phonon transport. *Nature Nanotechnology*, Nature Publishing Group UK London, v. 17, n. 9, p. 947–951, 2022.

20 CHERNATYNSKIY, A.; PHILLPOT, S. R. Evaluation of computational techniques for solving the boltzmann transport equation for lattice thermal conductivity calculations. *Phys. Rev. B*, American Physical Society, v. 82, p. 134301, Oct 2010. Disponível em: <https://link.aps.org/doi/10.1103/PhysRevB.82.134301>.

21 LI, W.; CARRETE, J.; A. Katcho, N.; MINGO, N. Shengbte: A solver of the boltzmann transport equation for phonons. *Computer Physics Communications*, v. 185, n. 6, p. 1747–1758, 2014. ISSN 0010-4655. Disponível em: <https://www.sciencedirect.com/science/article/pii/S0010465514000484>.

22 HENRY, A. S.; CHEN, G. Spectral phonon transport properties of silicon based on molecular dynamics simulations and lattice dynamics. *Journal of Computational and Theoretical Nanoscience*, American Scientific Publishers, v. 5, n. 2, p. 141–152, 2008.

23 ZIMAN, J. *Electrons and Phonons: The Theory of Transport Phenomena in Solids*. Oxford University Press, 2001. ISBN 9780198507796. Disponível em: <https://doi.org/10.1093/acprof:oso/9780198507796.001.0001>.

24 KARPLUS, M.; PETSKO, G. A. Molecular dynamics simulations in biology. *Nature*, Springer, v. 347, p. 631–639, 1990.

25 GUNSTEREN, W. F. V.; BERENDSEN, H. J. Computer simulation of molecular dynamics: methodology, applications, and perspectives in chemistry. *Angewandte Chemie International Edition in English*, Wiley Online Library, v. 29, n. 9, p. 992–1023, 1990.

26 GISSINGER, J. R.; JENSEN, B. D.; WISE, K. E. Modeling chemical reactions in classical molecular dynamics simulations. *Polymer*, v. 128, p. 211–217, 2017. ISSN 0032-3861. Disponível em: <https://www.sciencedirect.com/science/article/pii/S0032386117309114>.

27 KONG, L. T. Phonon dispersion measured directly from molecular dynamics simulations. *Computer Physics Communications*, v. 182, n. 10, p. 2201–2207, 2011. ISSN 0010-4655. Disponível em: <https://www.sciencedirect.com/science/article/pii/S0010465511001500>.

28 BERNU, B.; HIWATARI, Y.; HANSEN, J. A molecular dynamics study of the glass transition in binary mixtures of soft spheres. *Journal of Physics C: Solid State Physics*, IOP Publishing, v. 18, n. 14, p. L371, 1985.

29 LAMBERTI, V. E.; FOSDICK, L. D.; JESSUP, E. R.; SCHAUBLE, C. J. A hands-on introduction to molecular dynamics. *Journal of chemical education*, ACS Publications, v. 79, n. 5, p. 601, 2002.

30 GOULD, H.; TOBOCHNIK, J.; CHRISTIAN, W. *An Introduction to Computer Simulation Methods Applications to Physical System*. 3. ed. [S.l.: s.n.], 2007.

31 TERSOFF, J. New empirical approach for the structure and energy of covalent systems. *Phys. Rev. B*, American Physical Society, v. 37, p. 6991–7000, Apr 1988. Disponível em: <https://link.aps.org/doi/10.1103/PhysRevB.37.6991>.

32 TERSOFF, J. Modeling solid-state chemistry: Interatomic potentials for multicomponent systems. *Phys. Rev. B*, American Physical Society, v. 39, p. 5566–5568, Mar 1989. Disponível em: <https://link.aps.org/doi/10.1103/PhysRevB.39.5566>.

33 FAN, Z.; WANG, Y.; GU, X.; QIAN, P.; SU, Y.; ALA-NISSILA, T. A minimal tersoff potential for diamond silicon with improved descriptions of elastic and phonon transport properties. *Journal of Physics: Condensed Matter*, IOP Publishing, v. 32, n. 13, p. 135901, dec 2019. Disponível em: <https://dx.doi.org/10.1088/1361-648X/ab5c5f>.

34 BAZANT, M. Z.; KAXIRAS, E.; JUSTO, J. F. Environment-dependent interatomic potential for bulk silicon. *Physical Review B*, APS, v. 56, n. 14, p. 8542, 1997.

35 BERENDSEN, H. J.; POSTMA, J. v.; GUNSTEREN, W. F. V.; DINOLA, A.; HAAK, J. R. Molecular dynamics with coupling to an external bath. *The Journal of chemical physics*, American Institute of Physics, v. 81, n. 8, p. 3684–3690, 1984.

36 LEMAK, A.; BALABAEV, N. On the berendsen thermostat. *Molecular Simulation*, Taylor & Francis, v. 13, n. 3, p. 177–187, 1994.

37 NOSÉ, S. A unified formulation of the constant temperature molecular dynamics methods. *The Journal of chemical physics*, American Institute of Physics, v. 81, n. 1, p. 511–519, 1984.

38 HOOVER, W. G. Canonical dynamics: Equilibrium phase-space distributions. *Phys. Rev. A*, American Physical Society, v. 31, p. 1695–1697, Mar 1985. Disponível em: <https://link.aps.org/doi/10.1103/PhysRevA.31.1695>.

39 MARTYNA, G. J.; KLEIN, M. L.; TUCKERMAN, M. Nosé–hoover chains: The canonical ensemble via continuous dynamics. *The Journal of chemical physics*, American Institute of Physics, v. 97, n. 4, p. 2635–2643, 1992.

40 SCHNEIDER, T.; STOLL, E. Molecular-dynamics study of a three-dimensional one-component model for distortive phase transitions. *Phys. Rev. B*, American Physical Society, v. 17, p. 1302–1322, Feb 1978. Disponível em: <https://link.aps.org/doi/10.1103/PhysRevB.17.1302>.

41 BUSSI, G.; DONADIO, D.; PARRINELLO, M. Canonical sampling through velocity rescaling. *The Journal of Chemical Physics*, v. 126, n. 1, p. 014101, 01 2007. ISSN 0021-9606. Disponível em: <https://doi.org/10.1063/1.2408420>.

42 KE, Q.; GONG, X.; LIAO, S.; DUAN, C.; LI, L. Effects of thermostats/barostats on physical properties of liquids by molecular dynamics simulations. *Journal of Molecular Liquids*, v. 365, p. 120116, 2022. ISSN 0167-7322. Disponível em: <https://www.sciencedirect.com/science/article/pii/S0167732222016555>.

43 MCQUARRIE, D. A. *Statistical Mechanics*. [S.l.]: Harper Collins, 1976. (Harper's chemistry series).

44 IKESHOJI, T.; HAFSKJOLD, B. Non-equilibrium molecular dynamics calculation of heat conduction in liquid and through liquid-gas interface. *Molecular Physics*, Taylor & Francis, v. 81, n. 2, p. 251–261, 1994. Disponível em: <https://doi.org/10.1080/00268979400100171>.

45 MüLLER-PLATHE, F. A simple nonequilibrium molecular dynamics method for calculating the thermal conductivity. *The Journal of Chemical Physics*, v. 106, n. 14, p. 6082–6085, 1997. Disponível em: <https://doi.org/10.1063/1.473271>.

46 EVANS, D. J. Homogeneous nemd algorithm for thermal conductivity—application of non-canonical linear response theory. *Physics Letters A*, v. 91, n. 9, p. 457–460, 1982. ISSN 0375-9601. Disponível em: <https://www.sciencedirect.com/science/article/pii/0375960182907484>.

47 FAN, Z.; DONG, H.; HARJU, A.; ALA-NISSILA, T. Homogeneous nonequilibrium molecular dynamics method for heat transport and spectral decomposition with many-body potentials. *Physical Review B*, APS, v. 99, n. 6, p. 064308, 2019.

48 EVANS DENIS J.;MORRIS, G. P. *Statistical Mechanics of Non Equilibrium Liquids*. [S.l.]: ANU E Press, 2007. (Harper's chemistry series).

49 SÄÄSKILAHTI, K.; OKSANEN, J.; VOLZ, S.; TULKKI, J. Frequency-dependent phonon mean free path in carbon nanotubes from nonequilibrium molecular dynamics. *Physical Review B*, APS, v. 91, n. 11, p. 115426, 2015.

50 FAN, Z.; PEREIRA, L. F. C.; WANG, H.-Q.; ZHENG, J.-C.; DONADIO, D.; HARJU, A. Force and heat current formulas for many-body potentials in molecular dynamics simulations with applications to thermal conductivity calculations. *Physical Review B*, APS, v. 92, n. 9, p. 094301, 2015.

51 ZHOU, Y.; ZHANG, X.; HU, M. Quantitatively analyzing phonon spectral contribution of thermal conductivity based on nonequilibrium molecular dynamics simulations. i. from space fourier transform. *Physical Review B*, APS, v. 92, n. 19, p. 195204, 2015.

52 THOMPSON, A. P.; AKTULGA, H. M.; BERGER, R.; BOLINTINEANU, D. S.; BROWN, W. M.; CROZIER, P. S.; VELD, P. J. in 't; KOHLMEYER, A.; MOORE, S. G.; NGUYEN, T. D.; SHAN, R.; STEVENS, M. J.; TRANCHIDA, J.; TROTT, C.; PLIMPTON, S. J. LAMMPS - a flexible simulation tool for particle-based materials modeling at the atomic, meso, and continuum scales. *Comp. Phys. Comm.*, v. 271, p. 108171, 2022.

53 FAN, Z.; CHEN, W.; VIERIMAA, V.; HARJU, A. Efficient molecular dynamics simulations with many-body potentials on graphics processing units. *Computer Physics Communications*, v. 218, p. 10–16, 2017. ISSN 0010-4655. Disponível em: <https://www.sciencedirect.com/science/article/pii/S0010465517301339>.

54 STANDARDS, N. I. of; TECHNOLOGY. *CODATA Value: lattice parameter of Silicon*. 2018. Disponível em: <https://physics.nist.gov/cgi-bin/cuu/Value?asil>.

55 PEREIRA, L. F. C.; SAVIĆ, I.; DONADIO, D. Thermal conductivity of one-, two-and three-dimensional sp2 carbon. *New journal of physics*, IOP Publishing, v. 15, n. 10, p. 105019, 2013.

56 C. Pereira, L. F. Investigating mechanical properties and thermal conductivity of 2d carbon-based materials by computational experiments. *Computational Materials Science*, v. 196, p. 110493, 2021. ISSN 0927-0256. Disponível em: <https://www.sciencedirect.com/science/article/pii/S0927025621002184>.

57 VOLZ, S. G.; CHEN, G. Molecular-dynamics simulation of thermal conductivity of silicon crystals. *Physical Review B*, APS, v. 61, n. 4, p. 2651, 2000.

58 FAN, Z.; PEREIRA, L. F. C.; HIRVONEN, P.; ERVASTI, M. M.; ELDER, K. R.; DONADIO, D.; ALA-NISSILA, T.; HARJU, A. Thermal conductivity decomposition in two-dimensional materials: application to graphene. *Physical Review B*, APS, v. 95, n. 14, p. 144309, 2017.

59 LI, Z.; XIONG, S.; SIEVERS, C.; HU, Y.; FAN, Z.; WEI, N.; BAO, H.; CHEN, S.; DONADIO, D.; ALA-NISSILA, T. Influence of thermostatting on nonequilibrium molecular dynamics simulations of heat conduction in solids. *The Journal of chemical physics*, AIP Publishing, v. 151, n. 23, 2019.

60 SCHELLING, P. K.; PHILLPOT, S. R.; KEBLINSKI, P. Comparison of atomic-level simulation methods for computing thermal conductivity. *Physical Review B*, APS, v. 65, n. 14, p. 144306, 2002.

61 HOPKINS, P. E.; REINKE, C. M.; SU, M. F.; III, R. H. O.; SHANER, E. A.; LESEMAN, Z. C.; SERRANO, J. R.; PHINNEY, L. M.; EL-KADY, I. Reduction in the thermal conductivity of single crystalline silicon by phononic crystal patterning. *Nano letters*, ACS Publications, v. 11, n. 1, p. 107–112, 2011.